

## MIT Open Access Articles

*Influence of Transonic Flutter on the Conceptual Design of Next-Generation Transport Aircraft*

The MIT Faculty has made this article openly available. **Please share** how this access benefits you. Your story matters.

**As Published:** 10.2514/1.J057302

**Publisher:** American Institute of Aeronautics and Astronautics (AIAA)

**Persistent URL:** <https://hdl.handle.net/1721.1/136533>

**Version:** Author's final manuscript: final author's manuscript post peer review, without publisher's formatting or copy editing

**Terms of use:** Creative Commons Attribution-Noncommercial-Share Alike



# Influence of Transonic Flutter on the Conceptual Design of Next-Generation Transport Aircraft

Max M. J. Opgenoord\* and Mark Drela†

*Massachusetts Institute of Technology, Cambridge, Massachusetts 02139*

Karen E. Willcox‡

*University of Texas at Austin, Austin, Texas 78712*

Transonic aeroelasticity is an important consideration in the conceptual design of next-generation aircraft configurations. This paper develops a low-order physics-based flutter model for swept high-aspect-ratio wings. The approach builds upon a previously developed flutter model that uses the flowfield's lowest moments of vorticity and volume-source density perturbations as its states. The contribution of this paper is a new formulation of the model for swept high-aspect-ratio wings. The aerodynamic model is calibrated using off-line 2D unsteady transonic CFD simulations. Combining that aerodynamic model with a beam model results in a low-dimensional overall aeroelastic system. The low computational cost of the model permits its incorporation in a conceptual design tool for next-generation transport aircraft. The model's capabilities are demonstrated by finding transonic flutter boundaries for different clamped wing configurations, and investigating the influence of transonic flutter on the planform design of next-generation transport aircraft.

## Nomenclature

$\mathcal{R}$	= Aspect ratio
$\mathbf{A}_a, \mathbf{B}_a$	= State-space matrices of aerodynamic system
$A_\Gamma, A_{\dot{\Gamma}}, A_\kappa$	= Coefficients of $\Gamma$ evolution equation
$B_\Gamma, B_\kappa, B_{\dot{\kappa}}$	= Coefficients of $\kappa_x$ evolution equation
$C_{th}(\bar{\omega})$	= Theodorsen's function
$EI$	= Bending stiffness
$GJ$	= Torsional stiffness
$I_{\bar{y}}$	= Mass moment of inertia per span around elastic axis
$L$	= Lift per span
$L_c$	= Circulatory lift
$L_{nc}$	= Non-circulatory lift
$\mathcal{M}$	= Internal bending moment
$M_\infty$	= Freestream Mach number
$M_{CR}$	= Cruise Mach number
$M_{ea}$	= Aerodynamic moment per span around elastic axis
$M_{nc}$	= Non-circulatory moment around the elastic axis
$\mathcal{S}$	= Internal shear force
$S_{\bar{y}}$	= Mass unbalance per span
$\mathcal{T}$	= Internal torsion moment
$\mathbf{V}$	= Velocity field
$V_\mu$	= Flutter speed index
$V_\infty$	= Freestream velocity
$V_\perp$	= Wing-perpendicular velocity
$\mathbf{a}$	= Acceleration

\*Postdoctoral Research Associate, Department of Aeronautics and Astronautics; mopg@mit.edu. Student member AIAA.

†Terry J. Kohler Professor of Aeronautics and Astronautics; drela@mit.edu. Fellow AIAA.

‡Director, Institute of Computational Engineering and Sciences; kwillcox@ices.utexas.edu. Associate Fellow AIAA.

$b$	=	Wing span
$c$	=	Airfoil chord length
$c_{\ell_0}$	=	Baseline sectional lift coefficient
$d$	=	Distance between quarter-chord and elastic axis
$h$	=	Vertical position, positive downward
$h_a$	=	Altitude
$\bar{l}$	=	Effective wing length
$m$	=	Mass per span
$n_{\text{beam}}$	=	Number of beam nodes
$p(y)$	=	Parameterized span loading
$r_\theta$	=	Radius of gyration per span about the elastic axis
$t$	=	Time
$\mathbf{u}_a$	=	State-space control vector of aerodynamic system
$x, y, z$	=	Aircraft coordinate system
$\bar{x}, \bar{y}, \bar{z}$	=	Coordinates aligned with swept wing
$\mathbf{x}_a$	=	State-space vector of aerodynamic system
$x_{\text{cg}}$	=	Position of center of gravity relative to wing leading edge
$x_{\text{ea}}$	=	Position of elastic axis relative to wing leading edge
$w$	=	Vertical (downward) velocity
$\Gamma$	=	Circulation strength
$\gamma$	=	Local dihedral angle
$\theta$	=	Pitch angle
$\kappa_x$	=	$x$ -doublet strength
$\Lambda$	=	Sweep angle
$\lambda$	=	Taper ratio
$\mu$	=	Apparent mass ratio
$\sigma$	=	Volume-source strength
$\rho_\infty$	=	Free stream density
$\tau$	=	Thickness ratio of airfoil
$\chi_{\text{fl}}$	=	Maximum real eigenvalue of aeroelastic system
$\omega$	=	Angular velocity
$\bar{\omega}$	=	Reduced frequency
$\omega_\theta, \omega_h$	=	Uncoupled in-vacuo natural frequencies in pitch and heave

## I. Introduction

NEXT-GENERATION transport aircraft typically feature high-aspect-ratio wings—examples being the Truss-Braced Wing concept [1] or D8.x aircraft [2]—which are more susceptible to flutter. Such high-aspect-ratio wings increase the aerodynamic efficiency, but are also more flexible, leading to more associated aeroelasticity problems. Flutter therefore becomes an even more important design consideration for these aircraft concepts, and requires flutter constraints to be included in the design of these aircraft as early as possible, preferably in the conceptual design stage. Doing so will prevent costly design changes in later design phases, or during flight testing. However, these aircraft fly in the transonic flow regime, which introduces complicated aeroelastic behavior that is hard to capture with existing tools suitable for early design exploration. Such existing methods employ linear models that, when extrapolated to the transonic flow regime, can yield optimistic estimates and thus are ineffective at imposing the required design constraints. This paper therefore develops a new physics-based wing flutter assessment capability for aircraft in transonic flow that is suitable for incorporation in early-stage conceptual design studies.

When a wing in transonic flow deforms, shocks move over the surface of the wing [3], which leads to complex aeroelasticity phenomena. An example of such intricate transonic flutter behavior is the transonic dip, which has been observed and described in detail by many researchers [4–6]. It is also commonly accepted that linear flutter theories cannot capture this transonic dip behavior accurately [7–9]. As we show later in the paper, this inaccuracy in linear flutter models can have a large influence on the conceptual design of next-generation transport aircraft.

The theory of flutter behavior of wings has been investigated extensively for decades now, especially for incompressible, subsonic, and supersonic flow. Theodorsen [10], for instance, considered flutter of a uniform, straight wing in

incompressible flow. Barmby et al. [11] extended Theodorsen's theory to swept wings in incompressible flow. Yates extended this theory to subsonic, supersonic and hypersonic flow—the method loses accuracy for transonic flow—with a modified strip theory and validated the theoretical results with experimental results [12].

Flutter prediction in transonic flow has typically relied on high-fidelity unsteady CFD simulations [13, 14]. These CFD models can accurately resolve the key nonlinear features of the flow, but they are too expensive to use in an early design stage where a designer may wish to evaluate thousands of potential designs. To alleviate this cost, several approaches exist in which two-dimensional CFD solutions are combined with strip theory to assess the flutter behavior of wings [15]—but this is still too expensive to use in early-stage design. Aerodynamic influence coefficient (AIC) approaches [16] have also been proposed as a way to reduce the cost of CFD but their uses in the literature show a limited ability to incorporate parameterization and thus they too have seen limited integration in early-stage design tools. Detailed design studies therefore typically rely on linear flutter prediction methods using the Prandtl-Glauert transformation to account for compressibility [17, 18], but theoretically this is invalid for transonic flow.

Thus, there exists a need for a flutter model that is cheap enough to allow for potentially thousands of flutter evaluations of wing designs in the conceptual design phase, but at the same time is accurate enough to capture design trade-offs for commercial transport aircraft operating in the transonic flow regime. We therefore develop a physics-based transonic flutter model for swept aircraft wings and implement it in a physics-based conceptual aircraft design tool. The transonic flutter model builds upon a previously developed and validated airfoil flutter model [19], which is made applicable to high-aspect-ratio wings through strip theory and sweep correction (Section II). The model is validated for a pitching and heaving wing and for the flutter behavior of a 3D benchmark case (Section III). The flutter model is included in a physics-based conceptual design tool to describe the influence of transonic flutter on aircraft design (Section IV). The model is then used to describe the effect of several different wing configurations on flutter behavior of clamped wings (Section V). The model is also used to highlight the large influence of transonic flutter on the overall aircraft design of next-generation transport aircraft (Section VI).

## II. Wing Flutter Model

The aerodynamic model used in the wing flutter model is based on a physics-based aerodynamic model for unsteady transonic flow (Section II.A). This airfoil aerodynamic model is made applicable to wings through strip theory and sweep corrections (Section II.B). This wing aerodynamic model is then coupled to a beam model (Section II.C) to compute flutter characteristics of aircraft wings.

### II.A. Airfoil Transonic Flutter Model

Our physics-based model is derived from first principles of transonic unsteady flow, and this model's unknown coefficients are calibrated with high-fidelity unsteady 2D CFD simulations using Dynamic Mode Decomposition [20]. The approach for constructing that low-order model is shown in Fig. 1.

The low-order model uses as its aerodynamic state variables the circulation perturbation  $\Delta\Gamma$  and  $x$ -doublet perturbation  $\Delta\kappa_x$ , where the perturbations are defined relative to their steady transonic flow values. With these state variables, the aerodynamic state-space model can be written as [19],

$$\frac{d}{dt} \begin{bmatrix} \Delta\Gamma(t) \\ \Delta\kappa_x(t) \\ \Delta\dot{\kappa}_x(t) \end{bmatrix} = \underbrace{\begin{bmatrix} -\frac{A_\Gamma}{A_\Gamma} & -\frac{A_\kappa}{A_\Gamma} & 0 \\ 0 & 0 & 1 \\ B_\Gamma & B_\kappa & B_{\dot{\kappa}} \end{bmatrix}}_{\mathbf{A}_a} \underbrace{\begin{bmatrix} \Delta\Gamma(t) \\ \Delta\kappa_x(t) \\ \Delta\dot{\kappa}_x(t) \end{bmatrix}}_{\mathbf{x}_a} + \underbrace{\begin{bmatrix} \frac{V_\infty}{A_\Gamma} & \frac{c/4}{A_\Gamma} & \frac{1}{A_\Gamma} \\ 0 & 0 & 0 \\ 0 & 0 & 0 \end{bmatrix}}_{\mathbf{B}_a} \underbrace{\begin{bmatrix} \Delta\theta(t) \\ \Delta\omega(t) \\ \Delta w(t) \end{bmatrix}}_{\mathbf{u}_a}, \quad (1)$$

where  $\Delta\theta$  is the pitch angle perturbation,  $\Delta\omega$  is the pitch rate perturbation,  $\Delta w$  is the vertical velocity perturbation,  $V_\infty$  is the freestream velocity, and  $c$  is the chord. The coefficients ( $A_\Gamma$ ,  $A_\Gamma$ ,  $A_\kappa$ ,  $B_\Gamma$ ,  $B_\kappa$ , and  $B_{\dot{\kappa}}$ ) are calibrated using high-fidelity CFD simulations. For the 2D aerodynamic model, these coefficients are calibrated as a function of freestream Mach number  $M_\infty$ , baseline lift coefficient  $c_{\ell_0}$ , and thickness ratio  $\tau$ . Note that this calibration only has to be done once (offline) for a given airfoil family, and can therefore be considered to be included in the cost of designing a new airfoil family.

For the airfoil flutter model, the aerodynamic model (1) is combined with a typical-section structural model which has four states – heave perturbation  $\Delta h$ , vertical velocity perturbation  $\Delta w$ , pitch angle perturbation  $\Delta\theta$ , and pitch rate perturbation  $\Delta\omega$  [21, 22]. This gives an aeroelastic state-space system with seven states ( $\Delta h$ ,  $\Delta\theta$ ,  $\Delta w$ ,  $\Delta\omega$  for the

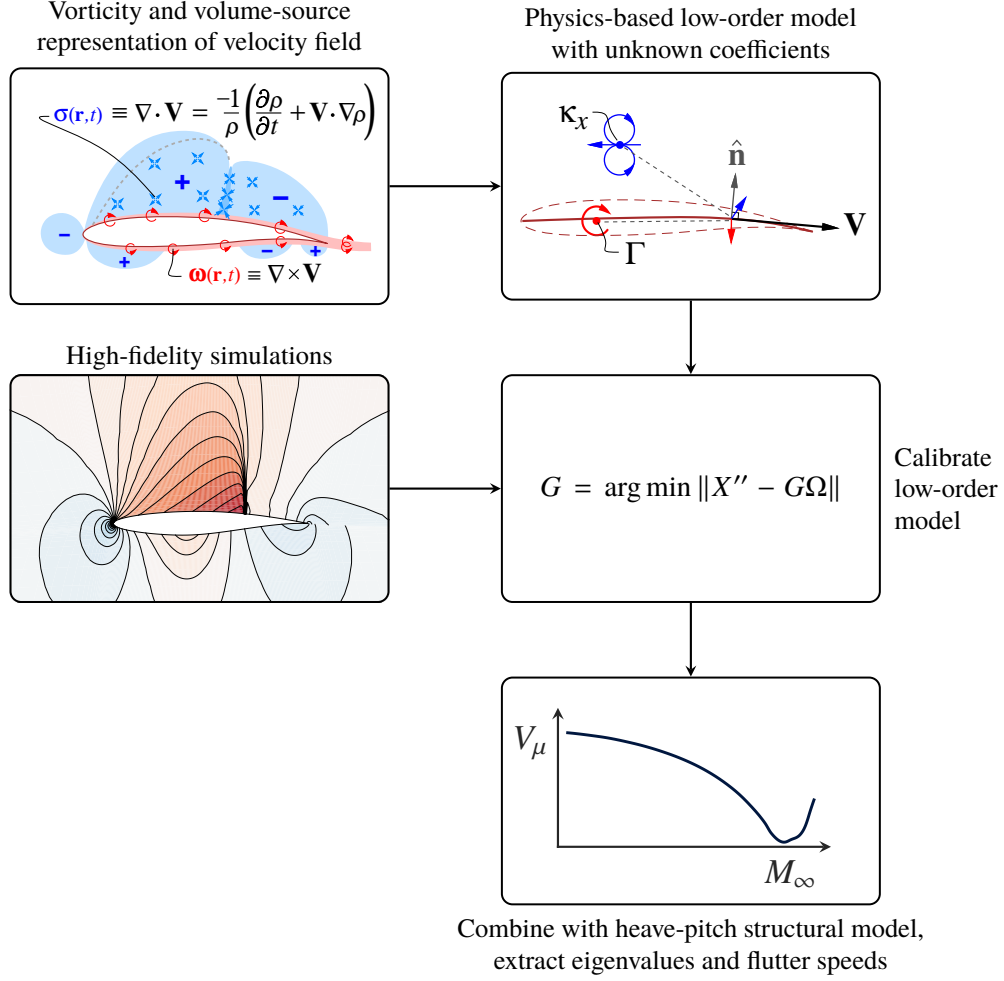


Fig. 1 Summary of transonic airfoil low-order flutter model construction, detailed in Ref. [19].

structural model;  $\Delta\Gamma$ ,  $\Delta\kappa_x$ ,  $\Delta\dot{\kappa}_x$  for the aerodynamic model). This model has been validated for a standard transonic flutter case in Ref. [19] and is shown to accurately characterize the transonic dip.

## II.B. Aerodynamic Model

Three ways to predict unsteady loads on an aircraft [23] are strip theory (2D unsteady airfoil theory with 3D corrections) [24, 25], the doublet-lattice method [26], and the unsteady vortex-lattice method (UVLM) [27, 28]. Considering that our goal is to investigate aircraft concepts with high-aspect-ratios, the use of strip theory here is appropriate. Using strip theory, the model described in Section II.A is used to assess the flutter characteristics of aircraft wings. For our model, this means that we use the perpendicular-plane Mach number  $M_\perp$  and lift coefficient  $c_{\ell_\perp}$  for selecting the appropriate coefficients for the transonic aerodynamics model.

Commercial transport aircraft commonly have swept wings to enable higher cruise Mach numbers. We consider the wing geometry in Fig. 2 with sweep angle  $\Lambda$ . The effective length of the wing  $\bar{l} = l/\cos \Lambda$ , and all section parameters such as chord length, moment of inertia, etc., are based on sections perpendicular to the elastic axis. We therefore assume that the elastic axis of the wing is straight.

For the aerodynamic model, we must account for the changes to the velocity distribution due to the swept wing. The vertical velocity at any point on the wing is found to be [11]

$$U_n(\bar{x}, t) = w + V_\infty \frac{\partial h}{\partial \bar{y}} \sin \Lambda + V_\infty \theta \cos \Lambda + \bar{x} \omega + \bar{x} V_\infty \frac{\partial \theta}{\partial \bar{y}} \sin \Lambda, \quad (2)$$

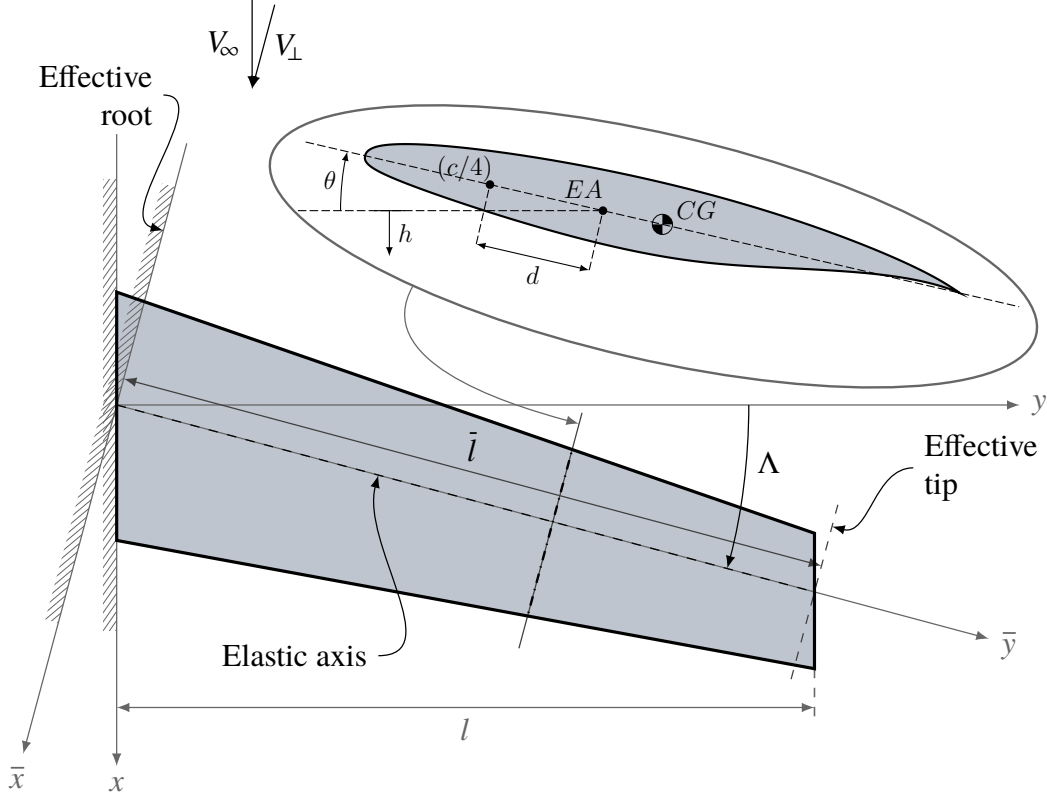


**Fig. 2** Swept wing considered in model. Figure adapted from Ref. [11, 19].

where  $\bar{x}$ ,  $\bar{y}$  are the coordinates aligned with the swept wing. From Eq. (2), Barmby et al. [11] found the circulatory lift per unit span for swept wings in incompressible flow to be

$$L_c = \pi \rho V_{\perp} c C_{th}(\bar{\omega}) \left[ w + V_{\perp} \frac{\partial h}{\partial \bar{y}} \tan \Lambda + V_{\perp} \theta + \frac{c}{4} \left( \omega + V_{\perp} \frac{\partial \theta}{\partial \bar{y}} \tan \Lambda \right) \right], \quad (3)$$

where  $V_{\perp}$  is the wing-perpendicular velocity and  $C_{th}(\bar{\omega})$  is Theodorsen's function [10] with  $\bar{\omega}$  the reduced frequency. Following the same approach, here the evolution equation for the circulation strength is defined to be,

$$\Delta \dot{\Gamma} = -\frac{A_{\Gamma}}{A_{\Gamma}} \Delta \Gamma - \frac{A_{\kappa}}{A_{\Gamma}} \Delta \kappa_x + \frac{1}{A_{\Gamma}} \left( \Delta w + V_{\perp} \frac{\partial \Delta h}{\partial \bar{y}} \tan \Lambda \right) + \frac{V_{\perp}}{A_{\Gamma}} \Delta \theta + \frac{c/4}{A_{\Gamma}} \left( \Delta \omega + V_{\perp} \frac{\partial \Delta \theta}{\partial \bar{y}} \tan \Lambda \right). \quad (4)$$

Lastly, the non-circulatory forces and moments used in the model are [11]

$$\Delta L_{nc} = \frac{1}{4} \pi \rho_{\infty} c^2 \left[ \Delta \dot{h} + V_{\perp} \frac{\partial \Delta \dot{h}}{\partial \bar{y}} \tan \Lambda + V_{\perp} \Delta \dot{\theta} \right] - \frac{1}{4} \pi \rho_{\infty} c^2 \left( x_{ea} - \frac{c}{2} \right) \left[ \Delta \ddot{\theta} + V_{\perp} \frac{\partial \Delta \dot{\theta}}{\partial \bar{y}} \right] \quad (5)$$

$$\begin{aligned} \Delta M_{nc} = & -\frac{1}{4} \pi \rho_{\infty} c^2 V_{\perp} \left[ \left( \frac{3}{4} c - x_{ea} \right) \Delta \dot{\theta} + \frac{1}{2} V_{\perp} \frac{\partial \Delta \dot{\theta}}{\partial \bar{y}} \tan \Lambda \right] - \frac{\rho_{\infty} \pi c^4}{128} \left[ \Delta \ddot{\theta} + V_{\perp} \frac{\partial \Delta \dot{\theta}}{\partial \bar{y}} \tan \Lambda \right] \\ & + \frac{1}{4} \rho_{\infty} \pi c^2 \left( x_{ea} - \frac{c}{2} \right) \left[ \Delta \dot{h} + V_{\perp} \frac{\partial \Delta \dot{h}}{\partial \bar{y}} \tan \Lambda - \left( x_{ea} - \frac{c}{2} \right) \left\{ \Delta \ddot{\theta} + V_{\perp} \frac{\partial \Delta \dot{\theta}}{\partial \bar{y}} \tan \Lambda \right\} \right]. \end{aligned} \quad (6)$$

Note that this formulation ignores the wing camber effect in the non-circulatory forces and moments, which is known to have a negligible effect on flutter [11].

Finally, note that—using the same assumptions as Barmby et al. [11]—this unsteady aerodynamics model ignores (1) variations in the trailing vorticity, (2) any variation of the airloads in the spanwise direction, and (3) any three-dimensional wing tip effects. These assumptions are quite reasonable for such high reduced frequencies, because in these cases the wake does not have time to newly form with each oscillation. Flutter is typically observed for high reduced frequencies, making these assumptions appropriate for this work.

### II.C. Wing Structural Model

For the structural part of the model, we use Bernoulli-Euler beam theory. Following Bisplinghoff et al. [21], the beam equations are,

$$m(\bar{y})\Delta\ddot{h}(\bar{y}, t) + S_{\bar{y}}(\bar{y})\Delta\ddot{\theta}(\bar{y}, t) + \frac{\partial^2}{\partial \bar{y}^2} \left[ EI(\bar{y}) \frac{\partial^2 \Delta h(\bar{y}, t)}{\partial \bar{y}^2} \right] = -\Delta L(\bar{y}, t) \quad (7a)$$

$$I_{\bar{y}}(\bar{y})\Delta\ddot{\theta}(\bar{y}, t) + S_{\bar{y}}(\bar{y})\Delta\ddot{h}(\bar{y}, t) - \frac{\partial}{\partial \bar{y}} \left[ GJ(\bar{y}) \frac{\partial \Delta \theta(\bar{y}, t)}{\partial \bar{y}} \right] = \Delta M_{\text{ea}}(\bar{y}, t) \quad (7b)$$

where  $m(\bar{y})$  is the mass per unit span,  $S_{\bar{y}}(\bar{y})$  is the mass unbalance per unit span,  $I_{\bar{y}}(\bar{y})$  is the mass moment of inertia per unit span,  $EI(\bar{y})$  is the bending stiffness, and  $GJ(\bar{y})$  is the torsional stiffness.  $L$  is the lift per unit span, and  $M_{\text{ea}}$  is the aerodynamic moment around the elastic axis per unit span. The boundary conditions for Eq. (7) are

$$\Delta h(0, t) = 0, \quad \frac{\partial \Delta h}{\partial \bar{y}}(0, t) = 0, \quad \frac{\partial^2 \Delta h}{\partial \bar{y}^2}(\bar{l}, t) = 0, \quad \frac{\partial^3 \Delta h}{\partial \bar{y}^3}(\bar{l}, t) = 0, \quad \Delta \theta(0, t) = 0, \quad \frac{\partial \Delta \theta}{\partial \bar{y}}(\bar{l}, t) = 0. \quad (7c)$$

The beam equations can be rewritten as

$$m(\bar{y})\Delta\ddot{h}(\bar{y}, t) - S_{\bar{y}}(\bar{y})\Delta\ddot{\theta}(\bar{y}, t) + \frac{\partial \Delta \mathcal{S}(\bar{y}, t)}{\partial \bar{y}} = -\Delta L(\bar{y}, t) \quad (8a)$$

$$I_{\bar{y}}(\bar{y})\Delta\ddot{\theta}(\bar{y}, t) + S_{\bar{y}}(\bar{y})\Delta\ddot{h}(\bar{y}, t) - \frac{\partial \Delta \mathcal{T}(\bar{y}, t)}{\partial \bar{y}} = \Delta M_{\text{ea}}(\bar{y}, t) \quad (8b)$$

where

$$\frac{\partial \Delta \mathcal{M}}{\partial \bar{y}} = \Delta \mathcal{S}, \quad \frac{\partial \Delta \gamma}{\partial \bar{y}} = \frac{\Delta \mathcal{M}}{EI}, \quad \frac{\partial \Delta h}{\partial \bar{y}} = \Delta \gamma, \quad \frac{\partial \Delta \theta}{\partial \bar{y}} = \frac{\Delta \mathcal{T}}{GJ}, \quad (8c)$$

with boundary conditions

$$\Delta h(0, t) = 0, \quad \Delta \gamma(0, t) = 0, \quad \Delta \mathcal{M}(\bar{l}, t) = 0, \quad \Delta \mathcal{S}(\bar{l}, t) = 0, \quad \Delta \theta(0, t) = 0, \quad \Delta \mathcal{T}(\bar{l}, t) = 0. \quad (8d)$$

To solve the system in Eq. (8), the wing is discretized in several sections, as shown in Fig. 3. The sectional properties are all computed using the assumed wing box shape as shown in Fig. 4. The thickness ratio  $\tau$  is used to determine the coefficients of the aerodynamic model, as explained in Section II.A. It is assumed that the elastic axis is at the center of the wing box. When the flutter model is used in a design setting, the wing box design variables such as spar and skin thicknesses are optimized in a conceptual design tool, and their values are then inputs to the flutter model.

The system in Eq. (8) is solved using finite differences, specifically the trapezoidal rule. However, Eq. (8) has  $6 \times n_{\text{beam}}$  structural parameters in the aeroelastic system, of which only two have inertial terms ( $\Delta h$  and  $\Delta \theta$ ). Such a large system slows down the eigenvalue computation. Instead, we can reduce the size of the system through Schur complements. Consider the discretized system of Eq. (8),

$$\bar{E} \begin{bmatrix} \Delta \ddot{\mathbf{h}} \\ \Delta \ddot{\gamma} \\ \Delta \ddot{\mathcal{M}} \\ \Delta \ddot{\mathcal{S}} \\ \Delta \ddot{\theta} \\ \Delta \ddot{\mathcal{T}} \end{bmatrix} + \bar{A} \begin{bmatrix} \Delta \mathbf{h} \\ \Delta \gamma \\ \Delta \mathcal{M} \\ \Delta \mathcal{S} \\ \Delta \theta \\ \Delta \mathcal{T} \end{bmatrix} = \begin{bmatrix} -\Delta \mathbf{L} \\ \mathbf{0} \\ \mathbf{0} \\ \mathbf{0} \\ \Delta \mathbf{M}_{\text{ea}} \\ \mathbf{0} \end{bmatrix}, \quad (9a)$$

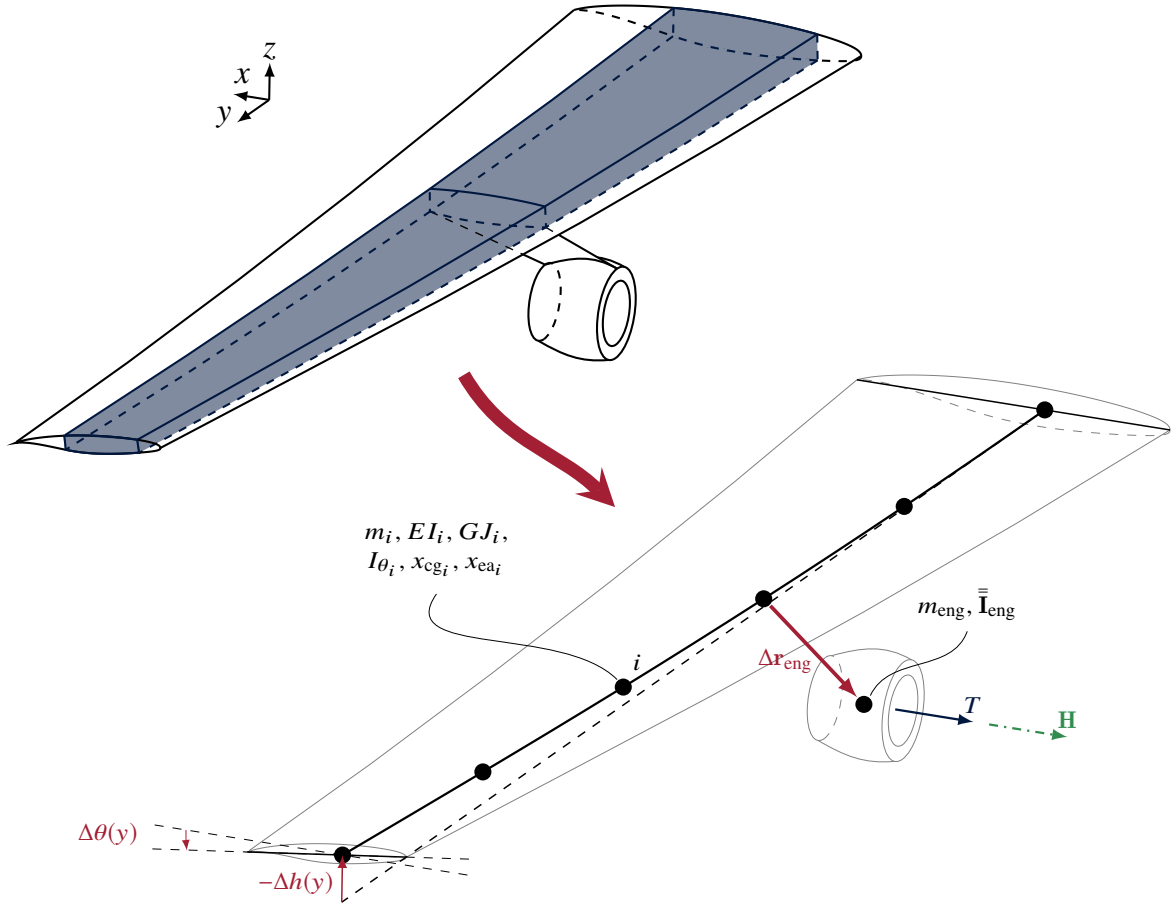


Fig. 3 Discretized beam model used in structural part of the flutter model.

where

$$\bar{\mathbf{E}} = \begin{bmatrix} \bar{\mathbf{E}}_{hh} & 0 & 0 & 0 & \bar{\mathbf{E}}_{h\theta} & 0 \\ 0 & 0 & 0 & 0 & 0 & 0 \\ 0 & 0 & 0 & 0 & 0 & 0 \\ 0 & 0 & 0 & 0 & 0 & 0 \\ \bar{\mathbf{E}}_{\theta h} & 0 & 0 & 0 & \bar{\mathbf{E}}_{\theta\theta} & 0 \\ 0 & 0 & 0 & 0 & 0 & 0 \end{bmatrix} \quad (9b)$$

$$\bar{\mathbf{A}} = \begin{bmatrix} 0 & 0 & 0 & \bar{\mathbf{A}}_{hS} & 0 & 0 \\ \bar{\mathbf{A}}_{\gamma h} & \bar{\mathbf{A}}_{\gamma\gamma} & 0 & 0 & 0 & 0 \\ 0 & \bar{\mathbf{A}}_{M\gamma} & \bar{\mathbf{A}}_{MM} & 0 & 0 & 0 \\ 0 & 0 & \bar{\mathbf{A}}_{SM} & \bar{\mathbf{A}}_{SS} & 0 & 0 \\ 0 & 0 & 0 & 0 & 0 & \bar{\mathbf{A}}_{\theta\tau} \\ 0 & 0 & 0 & 0 & \bar{\mathbf{A}}_{\tau\theta} & \bar{\mathbf{A}}_{\tau\tau} \end{bmatrix}. \quad (9c)$$

The matrices  $\bar{\mathbf{A}}_{\gamma h}$ ,  $\bar{\mathbf{A}}_{M\gamma}$ ,  $\bar{\mathbf{A}}_{SM}$ , and  $\bar{\mathbf{A}}_{\tau\theta}$  are all tightly banded and therefore cheap to invert. This allows for taking the





**Fig. 4 Wing box cross section.**

Schur complement of the system in Eq. (9) to obtain a system with only  $\mathbf{h}$ ,  $\theta$ ,

$$\begin{bmatrix} \mathbf{E}_{hh} & \mathbf{E}_{h\theta} \\ \mathbf{E}_{\theta h} & \mathbf{E}_{\theta\theta} \end{bmatrix} \begin{bmatrix} \Delta \ddot{\mathbf{h}} \\ \Delta \ddot{\theta} \end{bmatrix} + \begin{bmatrix} \mathbf{A}_{hh} & \mathbf{0} \\ \mathbf{0} & \mathbf{A}_{\theta\theta} \end{bmatrix} \begin{bmatrix} \Delta \mathbf{h} \\ \Delta \theta \end{bmatrix} = \begin{bmatrix} -\Delta \mathbf{L} \\ \Delta \mathbf{M}_{\text{ea}} \end{bmatrix}. \quad (10)$$

This structural model is then coupled to the aerodynamic model described in Section II.B through the aerodynamic lift and moment, yielding a  $7 \times n_{\text{beam}}$  descriptor state-space system.

The engine adds a large amount of inertia and mass to the wing, and it is therefore important to include in a flutter model. The engine is modeled as a point mass  $m_{\text{eng}}$  with inertia  $\bar{\mathbf{I}}_{\text{eng}}$  and angular momentum  $\mathbf{H}_{\text{eng}}$ , which are rotated into the swept coordinate system. As with the rest of the model, we only consider perturbations from the steady state. The thrust and moment generated by the engine are thus not taken into account.

The influence of the engine on the structural model comes through a discontinuity in  $\Delta \mathcal{S}$ ,  $\Delta \mathcal{M}$ , and  $\Delta \mathcal{T}$  at the section to which the engine is attached, as shown in Fig. 5. These discontinuities are captured with a zero-length grid interval at the engine attachment point.

The inertial-reaction forces and moments on the  $i$ th section on the wing due to the engine are [29]

$$\Delta \mathbf{F}_{\text{eng}} = -m_{\text{eng}} \Delta \mathbf{a}_{\text{eng}} \quad (11a)$$

$$\Delta \mathbf{M}_{\text{eng}} = \Delta \mathbf{r}_{\text{eng}} \times \Delta \mathbf{F}_{\text{eng}} - \Delta \boldsymbol{\omega}_i \times \mathbf{H}_{\text{eng}} - \bar{\mathbf{I}}_{\text{eng}} \Delta \dot{\boldsymbol{\omega}}_i - \Delta \boldsymbol{\omega}_i \times (\bar{\mathbf{I}}_{\text{eng}} \Delta \boldsymbol{\omega}_i), \quad (11b)$$

where  $\Delta \mathbf{r}_{\text{eng}} = [\Delta \bar{x}_{\text{eng}}, \Delta y_{\text{eng}}, \Delta z_{\text{eng}}]^T$  is the distance vector between the  $i$ th beam section and the engine, and  $\Delta \mathbf{F}_{\text{eng}}$  and  $\Delta \mathbf{M}_{\text{eng}}$  are the force and moment, respectively, on the  $i$ th beam section.  $\Delta \boldsymbol{\omega}_i$  is the rotation rate perturbation of the  $i$ th beam section with respect to the aircraft body axes, defined as  $\Delta \boldsymbol{\omega}_i = [-\Delta \dot{\gamma}, \Delta \dot{\theta}, 0]^T$ . We observe that  $\Delta \boldsymbol{\omega}_i \times \mathbf{H}_{\text{eng}}$  yields only an in-plane bending moment for unswept wings, while in-plane motion is not modeled here. Note that the last term in Eq. (11b) is a quadratic term in the perturbation rates, and can therefore be neglected. Finally,  $\Delta \mathbf{a}_{\text{eng}}$  is the inertial acceleration perturbation of the engine, defined as

$$\Delta \mathbf{a}_{\text{eng}} = \Delta \mathbf{a}_i + \Delta \dot{\boldsymbol{\omega}}_i \times \Delta \mathbf{r}_{\text{eng}} + \Delta \boldsymbol{\omega}_i \times (\Delta \boldsymbol{\omega}_i \times \Delta \mathbf{r}_{\text{eng}}) \quad (11c)$$

where  $\Delta \mathbf{a}_i$  is the acceleration perturbation of the  $i$ th beam section. Again, the last term in Eq. (11c) is a higher-order term in the perturbation rates and hence is omitted. Note that in this formulation, the aircraft fuselage is assumed to not participate significantly in the flutter modes.

The discontinuity in the shear force and bending moments results in additional terms in  $\mathbf{E}_{hh}$ ,  $\mathbf{E}_{h\theta}$ ,  $\mathbf{E}_{\theta h}$ , and  $\mathbf{E}_{\theta\theta}$  in Eq. (10).

### III. Validation of 3D Flutter Model

The accuracy of the flutter model is demonstrated by validating the two main simplifications for the flutter model: (1) using a physics-based low-order model in lieu of a full two-dimensional unsteady transonic flow simulation, and (2) using strip theory to extend a two-dimensional aerodynamic model to three dimensions. The accuracy of the physics-based low-order model has already been demonstrated in Ref. [19]. Strip theory is an accepted method for the aerodynamic response of high-aspect-ratio wings [24, 25] and thoroughly validated in the literature [30, 31]. Here, we further validate both simplifications by first comparing the computed aerodynamic response of a moderate aspect ratio wing in transonic flow against a high-fidelity unsteady 3D Euler simulation, and second by comparing its flutter predictions against experimental data for a well-known benchmark case. Our flutter model is shown to be at least as

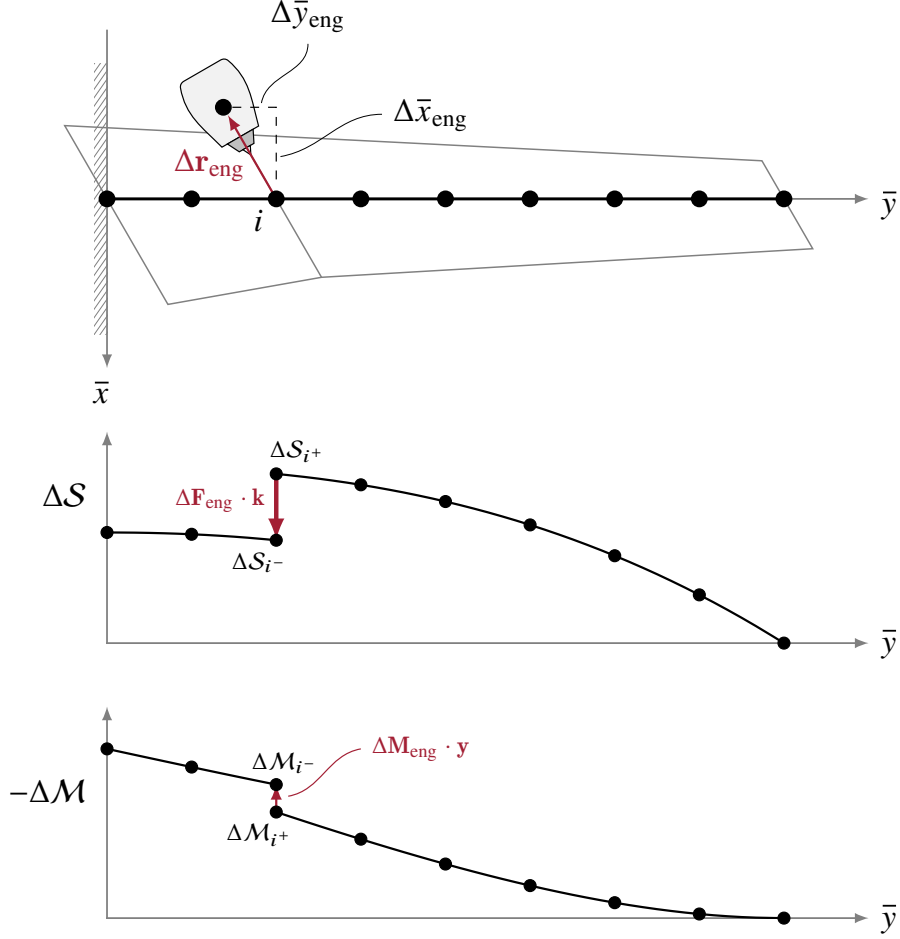


**Fig. 5** Inclusion of engine in beam model. Example curves for  $\Delta S$ ,  $\Delta M$  are shown for  $\ddot{h} < 0$ , note that a similar discontinuity is observed in  $\Delta \mathcal{T}$ .

accurate as more expensive, higher fidelity approaches, which—combined with the validation of the two-dimensional low-order model and many separate validation efforts for strip theory—provides enough support to allow for using the model in a design setting.

### III.A. Comparison with Pitching Wing

Here, we demonstrate the accuracy of the aerodynamic model on a wing with moderate aspect ratio. First, we calibrate the low-order model for the wing's airfoil—in this case the NASA SC(2)-0414 airfoil—using the methodology described in Section II.A and Ref. [19]. The results from this aerodynamic low-order model are then compared against the sectional lift coefficients obtained from a full 3D unsteady Euler simulation around the wing. The unsteady flow field around the wing is computed using SU2 [32].

A comparison between the low-order aerodynamic model and the SU2 solution is shown in Fig. 6 for  $M_\infty = 0.70$  and  $M_\infty = 0.75$ , both at  $\alpha = 0^\circ$ . At these conditions, the NASA SC(2)-0414 airfoil has a large supersonic region over the upper surface, as the critical Mach number for the NASA SC(2)-0414 airfoil at  $\alpha = 0^\circ$  is 0.648. The results in Fig. 6 show good agreement in both magnitude and phase.

### III.B. Flutter Prediction for Benchmark Supercritical Wing

The accuracy of the presented aeroelastic model is demonstrated using experimental results from the Benchmark Supercritical Wing (BSCW) [33]. The BSCW is also used for the Aeroelastic Prediction Workshop [34, 35]. The

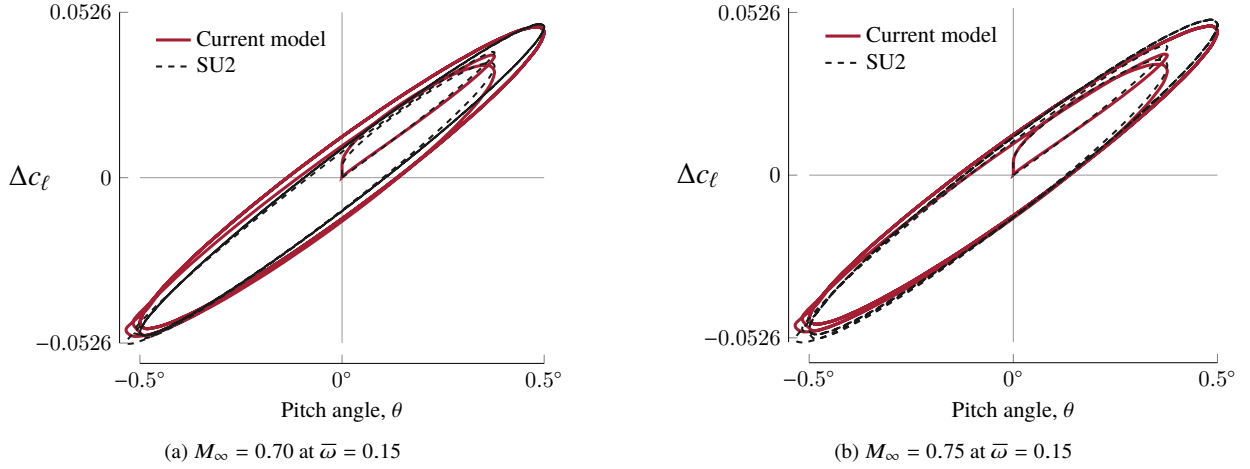


**Fig. 6** Sectional lift coefficient perturbation at 60% semispan versus pitch angle for a wing with a NASA SC(2)-0414 airfoil and  $R = 8$  at  $\alpha = 0^\circ$ .

BSCW wind tunnel model uses the NASA SC(2)-0414 airfoil and has no sweep or taper; further geometric parameters are described in Ref. [36]. Note that this model has an aspect ratio of 4, which is substantially lower than applications for which this flutter model is intended and thus the strip theory is expected to introduce a larger approximation error than it would for a higher aspect ratio case. The BSCW was chosen due to its relatively widespread use across the community as a benchmark problem and the availability of published results from several different groups.

The wind tunnel model was tested using the Pitch and Plunge Apparatus (PAPA) [37] in the NASA Langley Transonic Dynamics Tunnel. The model itself is rigid; all motion is therefore controlled by the PAPA. The appropriate structural model for this test case is therefore a typical section model, as also described in Ref. [19].

Fig. 7 shows a comparison between measured flutter speed indices at different Mach numbers and flutter speed indices found by our flutter model. For the low subsonic Mach numbers, the method agrees quite well with the experimental results. For high transonic Mach numbers ( $M_\infty > 0.80$ ), the fit is also reasonable. The flutter boundary from the presented method exhibits a sharper transonic dip, whereas the wind tunnel results barely show a transonic dip, however the errors are still within 5%–8%. Specifically for Case 2 of the AePW ( $M_\infty = 0.742$ ,  $\alpha = 0^\circ$ ), our method predicts a flutter speed 5.7% lower than the wind tunnel results (Fig. 8). However, we do note that the CFD results (full 3D unsteady RANS simulations) from the Aeroelastic Prediction Workshop shown in Figures 7 and 8 exhibit 5% or higher errors [38, 39]; thus our low-order model compares favorably with these high-fidelity benchmark results.

#### IV. Conceptual Aircraft Design Tool

As an illustration of how the flutter model can be incorporated into a conceptual design framework, we use the Transport Aircraft System OPTimization (TASOPT) [41] tool for the conceptual design of next-generation aircraft concepts. TASOPT was developed at MIT as part of a NASA project to design aircraft to meet aggressive fuel burn, noise, and emission reduction goals for the 2035 timeframe [42, 43]. To assess the performance of next-generation aircraft concepts, this conceptual design tool is primarily developed from first principles rather than using historical correlations. It uses low-order physical models implementing fundamental structural, aerodynamic, and thermodynamic theory, and relies on historical correlations only for the weight of secondary structure and aircraft equipment.

TASOPT can both size the aircraft for a particular mission (range and payload) and optimize the aircraft by varying, for instance, cruise altitude, cruise lift coefficient, aspect ratio, wing sweep, etc., to minimize mission fuel burn. TASOPT can therefore be used to model existing aircraft, assess their off-design performance, and perform a sensitivity analysis for an aircraft. TASOPT is also used to assess the influence of new technologies, such as advanced materials, on an airframe design. This tool is also used for the conceptual design of entirely new aircraft for a set of missions.

As with many aircraft conceptual design tools, dynamic aeroelasticity was not a design consideration in the initial version of TASOPT. To assess the influence of transonic flutter on the conceptual design of next-generation aircraft, the developed transonic flutter model is implemented in TASOPT here.

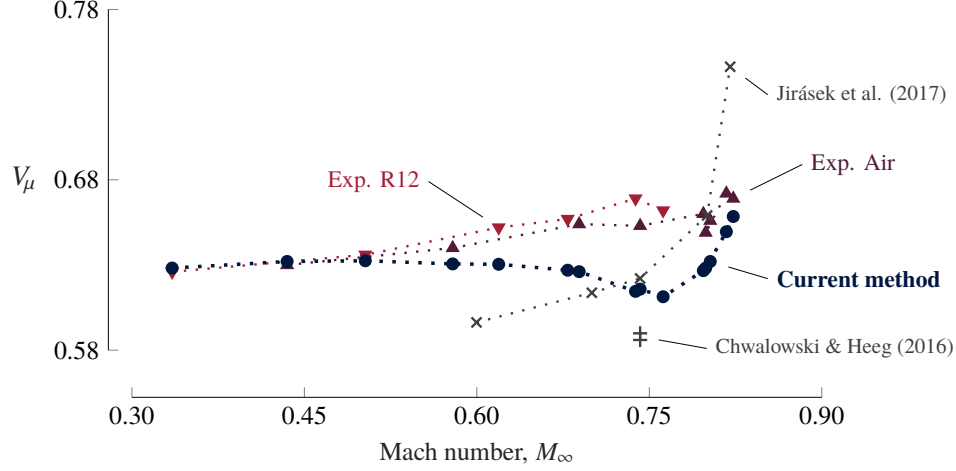


**Fig. 7** Comparison between experimental flutter points [33], flutter points found using CFD [38, 39] and flutter points found using the current method for the Benchmark Supercritical Wing at  $\alpha = 0^\circ$ .

	$V_\mu$	
Experimental (Air)	0.653	
Jirásek et al. (2017)	0.622	-4.75%
<b>Current method</b>	0.616	-5.67%
Chwalowski & Heeg (2016) (1)	0.590	-9.65%
Chwalowski et al. (2017)	0.587	-10.1%
Chwalowski & Heeg (2016) (2)	0.586	-10.2%

**Fig. 8** Difference in flutter speeds found by experiment [33], CFD [38–40], and our method for  $M_\infty = 0.742$ ,  $\alpha = 0^\circ$  (Case 2 from AePW).

Flutter is indicated using the eigenvalues of the aeroelastic system—the overall system that consists of the wing aerodynamics model and beam model. If the largest real part of the eigenvalues of the aeroelastic system—denoted here as  $\chi_{fl}$ —becomes positive, flutter occurs. Flutter constraints are included in a conceptual design tool by constraining the value of  $\chi_{fl}$  for several different points in the flight envelope.

The design routine in this conceptual design tool wraps an optimizer—the Nelder-Mead method [44]—around a weight-convergence routine. During the optimization several design parameters, such as cruise altitude, wing sweep, aspect ratio, etc., are varied to minimize the fleet-wide fuel energy consumption per payload-range. This outer optimization loop includes constraints on minimum balanced field length, fuel weight, and maximum wing span through penalty terms in the objective function [41]. The requirement for no flutter occurring for  $K$  operating points is also included via penalty terms on the real part of the eigenvalues associated with these operating points [45, 46]. The updated optimization problem is then

$$f(\mathbf{x}) = \underbrace{f_{\text{obj}}(\mathbf{x}) + v_{\text{BF}} \left\{ \max [0, l_{\text{BF}} - l_{\text{BF,max}}] \right\}^2}_{\text{existing objective and constraints}} + \dots + v_{\text{fl}} \underbrace{\sum_{k=1}^K \left\{ \max [0, \chi_{\text{fl},k} - \chi_{\text{fl,max}}] \right\}^2}_{\text{added flutter constraints}}, \quad (12)$$

where  $\mathbf{x}$  are the design variables,  $f(\mathbf{x})$  is the overall objective function,  $f_{\text{obj}}(\mathbf{x})$  is the original objective function (mission fuel burn) and  $l_{\text{BF}}$  is the balanced field length.  $v_{\text{BF}}$  and  $v_{\text{fl}}$  are suitable weighting factors for the balance field length constraint and the flutter constraints, respectively.  $\chi_{\text{fl},k}$  is largest real part of the eigenvalues of the aeroelastic system for the  $k$ th operating point, and  $\chi_{\text{fl,max}}$  is the largest value tolerated, typically  $-0.005/\text{s}$ .

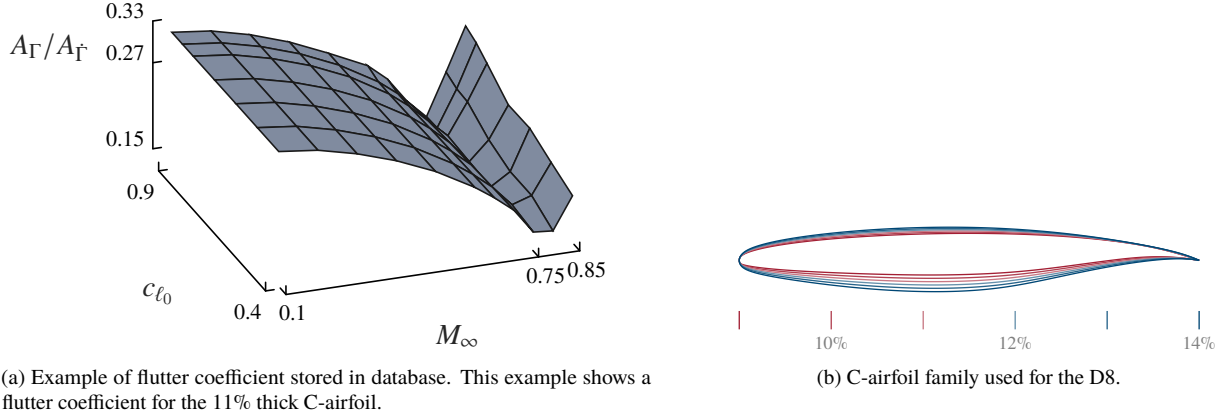


**Fig. 9** A database of flutter coefficients is generated for an airfoil family as a function of  $M_\perp$ ,  $c_{\ell_0}$ , and  $\tau$ .

The flutter model is included in TASOPT using a database of flutter coefficients with  $c_{\ell_0}$ ,  $M_\perp$ ,  $\tau$  as the database independent variables. We calibrate 2D low-order models, using the methodology described in Section II.A, for several thickness ratios  $\tau$  of an airfoil family (Fig. 9b) at different baseline lift coefficients  $c_{\ell_0}$  and Mach numbers  $M_\perp$  and store these in a database. An example of how such a flutter coefficient varies with  $c_{\ell_0}$  and  $M_\perp$  is shown in Fig. 9a. Whenever TASOPT queries a flutter evaluation, the appropriate flutter coefficients are found through spline interpolation using the flutter coefficient database.

TASOPT uses a parameterized spanwise loading  $p(y)$ , whose shape is either specified, or optimized for the best tradeoff between structural weight and induced drag (computed via a Trefftz-Plane analysis). Here, this same loading is used to obtain the local lift coefficient,

$$c_{\ell_\perp}(\bar{y}) = \frac{2p(\bar{y}) \cos \Lambda}{\rho_\infty V_\perp^2 c_\perp(\bar{y})}, \quad (13)$$

where  $c_\perp(\bar{y})$  is the local chord length perpendicular to the elastic axis. The wing-perpendicular quantities  $c_{\ell_\perp}$  and  $M_\perp$  are then used to get the appropriate flutter model for each section of the wing using the flutter coefficient database.

## V. Influence of Wing Geometry on Transonic Flutter Boundaries

The flutter model explained in Section II is used here to quantify the influence of several parameters of an aircraft wing on the flutter boundary. Flutter crucially depends on phase differences between system degrees of freedom and aerodynamic forces and moments. Since the  $\kappa_x(t)$  phase strongly changes from subsonic to transonic flow [19], it is expected that transonic flow has a large influence on flutter behavior. To quantify this influence for various wing geometries, we compute the flutter boundary of a clamped wing in a wind tunnel-like set-up in Section V.A. We also couple the flutter model with TASOPT to evaluate the influence of the wing parameters on the flutter damping values in Section V.B where each aircraft on the flutter boundary is a weight-converged aircraft design.\*

### V.A. Clamped Wing

We consider a wind tunnel-like set-up for a straight, swept, tapered wing (Fig. 10). This problem has twelve nondimensional parameters, which are listed in Table 1.

\*Note that we do not make any claims on the general applicability of these trends; the onset of flutter is sensitive to small changes in the wing parameters and the results described herein only apply to the particular nondimensional parameters of the models described.

**Table 1** Nondimensional parameters for straight, swept, tapered wing.

Parameter		Parameter	
$\mathcal{R}$	Aspect ratio	$\Lambda$	Sweep angle
$M_\infty$	Freestream Mach number	$(x_{ea}/c)$	Relative elastic axis position
$c_{\ell_0}$	Baseline lift coefficient	$(x_{cg}/c)$	Relative center of gravity position
$\tau$	Thickness ratio	$(\omega_\theta/\omega_h)$	Ratio of uncoupled pitch and heave frequencies
$\lambda$	Taper ratio	$\mu$	Apparent-mass ratio
$V_\mu$	Flutter speed index	$r_\theta$	Pitch radius of gyration per semi-chord ratio

The apparent-mass ratio  $\mu$ , flutter speed index  $V_\mu$ , and radius of gyration  $r_\theta^2$  are defined as,

$$\mu = \frac{4m_{\text{smc}}}{\pi\rho_\infty c_{\text{smc}}^2} \quad (14a)$$

$$V_\mu = \frac{2 V_\infty|_{\chi_{\text{fl}}=0}}{\sqrt{\mu}\omega_\theta c_{\text{smc}}} \quad (14b)$$

$$r_\theta^2 = \frac{4I_{\bar{y},\text{smc}}}{m_{\text{smc}}c_{\text{smc}}^2} \quad (14c)$$

where,

$$\omega_\theta = \sqrt{\frac{4(GJ)_{\text{smc}}}{m_{\text{smc}}b^2c_{\text{smc}}^2}} \quad (15a)$$

$$\omega_h = \sqrt{\frac{(EI)_{\text{smc}}}{m_{\text{smc}}b^4}}. \quad (15b)$$

These non-dimensional parameters determine the planform shape and sectional properties of the standard mean chord (SMC). To obtain the sectional properties over the entire wing, we scale the sectional properties with the local chord length:  $m \sim c^2$ ,  $I_{\bar{y}} \sim c^4$ ,  $EI \sim c^4$ , and  $GJ \sim c^4$ .

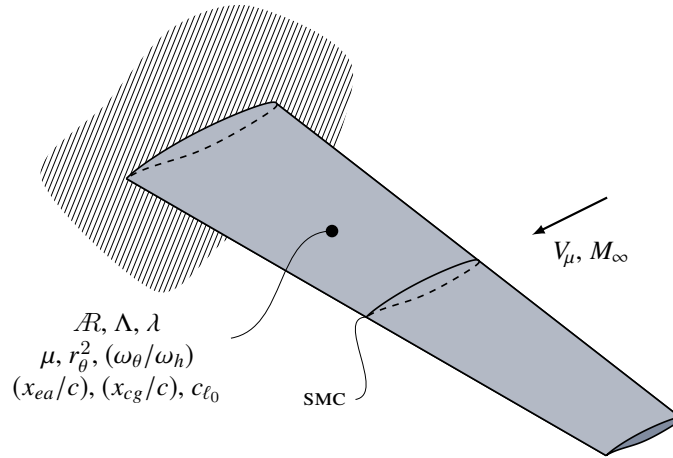


**Fig. 10** Geometry for clamped straight swept tapered wing, including the nondimensional parameters of the problem.

First, we show the influence of wing taper on the flutter boundary (Fig. 11). It is observed that the flutter boundary as a function of Mach number is almost independent of  $M_\infty$  and the taper ratio only determines the offset, with wings having less taper more susceptible to flutter. This is expected, as taper moves the wing mass inboard and also increases the overall bending and torsional stiffnesses, thus increasing the natural frequency of the wing.

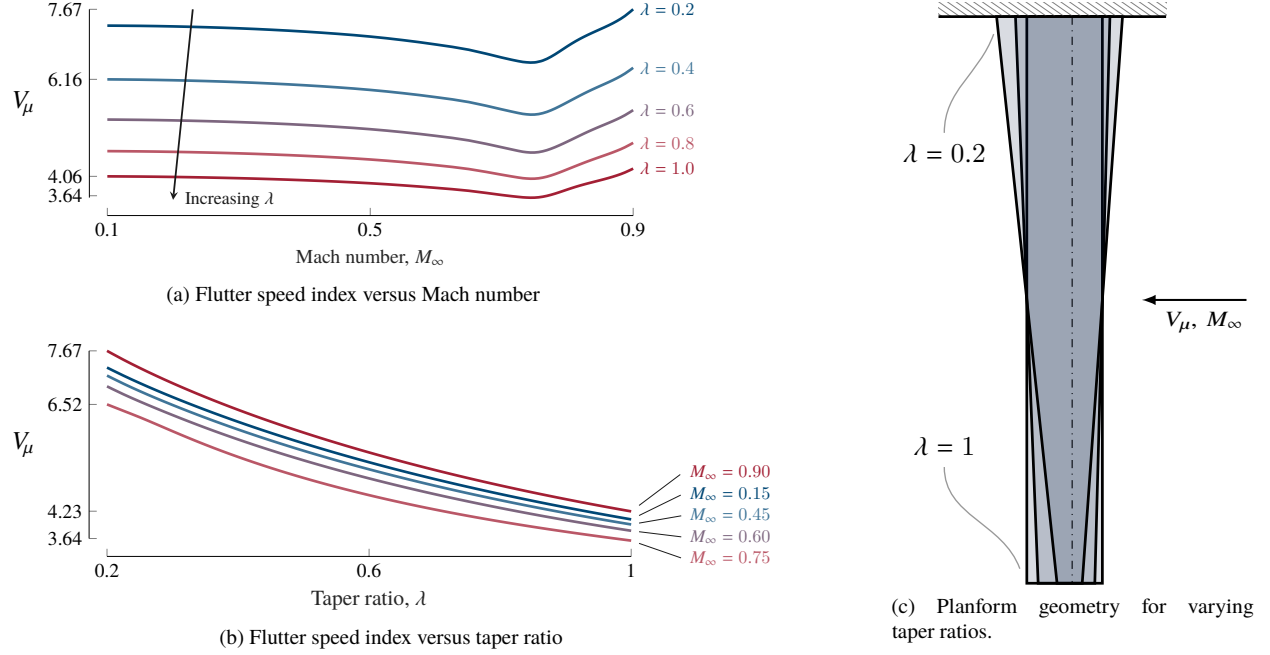


**Fig. 11 Influence of taper ratio on the flutter boundary for  $\mathcal{R} = 16$ ,  $\Lambda = 0^\circ$ ,  $\mu = 30$ ,  $\omega_\theta/\omega_h = 35$ ,  $r_\theta^2 = 0.15$ ,  $(x_{ea}/c) = 0.400$ ,  $(x_{cg}/c) = 0.401$ ,  $\tau = 0.13$ , and  $c_{\ell_0} = 0.6$  (C-airfoil family).**

The aspect ratio of the wing has a large influence on the flutter speed of the wing, which is a concern for next-generation aircraft designs. In order to look at a realistic variation of aspect ratio for an aluminum transport aircraft wing, we scale the properties of the wing as  $b \sim \sqrt{\mathcal{R}}$ ,  $c \sim 1/\sqrt{\mathcal{R}}$ ,  $h \sim 1/\sqrt{\mathcal{R}}$ ,  $m \sim \mathcal{R}$ ,  $GJ \sim 1$ ,  $EI \sim 1$ , and  $I_{\bar{y}} \sim 1$ . This ensures that the wing has a fixed wing area, fixed lift, and fixed wing box stress. Note that the nondimensional parameters are not kept constant with such a sweep over aspect ratio. Therefore we use the nondimensional parameters of  $\mathcal{R} = 15$  to scale the results.

The flutter boundary as a function of aspect ratio is shown in Fig. 12. We see that a higher aspect ratio reduces the flutter speed substantially, as expected. This influence does, however, plateau for high-aspect-ratios. Furthermore, the characteristic transonic dip is again observed.

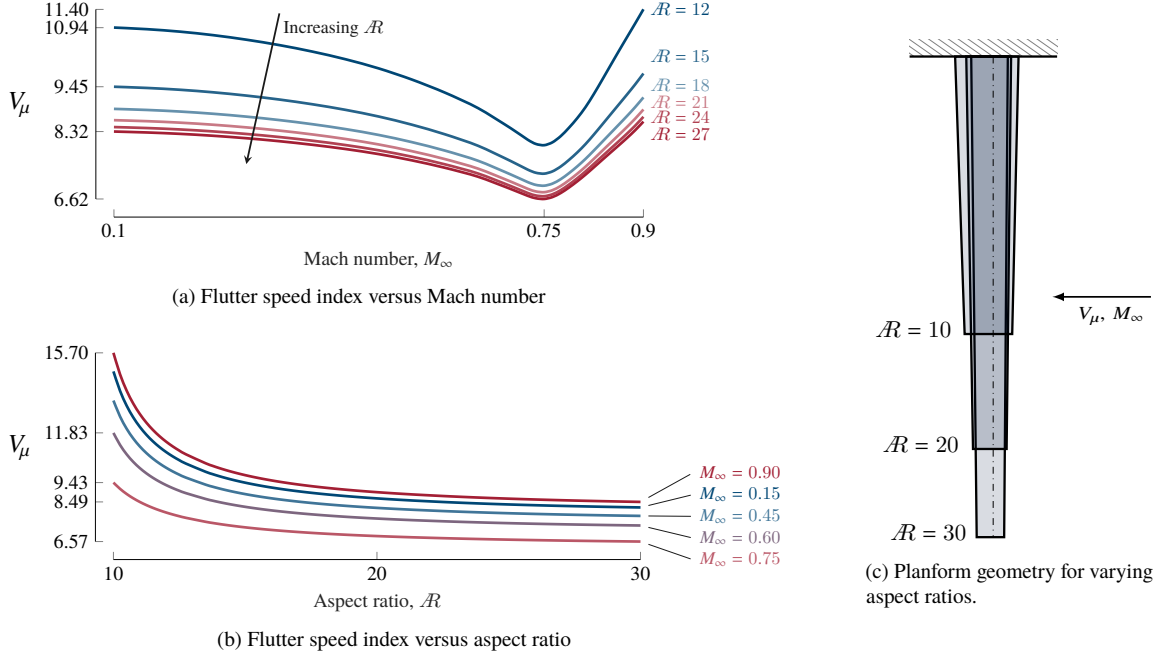


**Fig. 12 Influence of aspect ratio and freestream Mach number on the flutter boundary. The nondimensional parameters for  $R = 15$  are  $\Lambda = 0^\circ$ ,  $\lambda = 0.75$ ,  $\mu = 33$ ,  $\omega_\theta/\omega_h = 40$ ,  $r_\theta^2 = 0.125$ ,  $(x_{ea}/c) = 0.300$ ,  $(x_{cg}/c) = 0.301$ ,  $\tau = 0.13$ , and  $c_{\ell_0} = 0.6$  (C-airfoil family).**

The sweep of the wing has a profound effect on the flutter boundary, particularly for transonic flows because it lowers the wing-perpendicular Mach number. Wing sweep also couples the aerodynamic effects of displacement and twist, changing the phase differences between system degrees of freedom and aerodynamic forces and moments—it is therefore expected that sweep has a large influence on flutter behavior, especially in transonic flow. Flutter boundaries for various sweep angles and Mach numbers are shown in Fig. 13. We observe that for low subsonic Mach numbers the flutter boundary follows a shifted parabola for incompressible flows, similar to what was found by Barmby et al. [11]. That behavior changes completely for transonic flow, though. Fig. 13a clearly shows that wing sweep delays the transonic dip to higher freestream Mach numbers, which is partly the reason for a decrease in flutter speed for transonic Mach numbers. This delay is the result of a decrease in the wing-perpendicular Mach number as the sweep angle is increased. This is in fact the reason for sweeping the wing in the first place: to decrease the wing-perpendicular Mach number to decrease the wave drag. This delay in the transonic dip results in different behavior between subsonic and transonic flows: for low subsonic flows the sweep angle generally increases the flutter speed, whereas for transonic flows the sweep angle decreases the flutter speed (Fig. 13b).

When the engine is included in the model, additional nondimensional parameters need to be considered. Specifically, we consider the mass ratio of the engine  $\mu_{\text{eng}}$ , the radius of gyration of the engine  $\bar{r}_{\text{eng}}$ , the relative spanwise location of the engine  $\eta_{\text{eng}}$ , the relative chord-wise location of the engine  $\xi_{\text{eng},x}$ , and the relative normal location of the engine  $\xi_{\text{eng},z}$ . These parameters are defined as,

$$\mu_{\text{eng}} = \frac{m_{\text{eng}}}{m_{\text{smc}} b} \quad (16a)$$

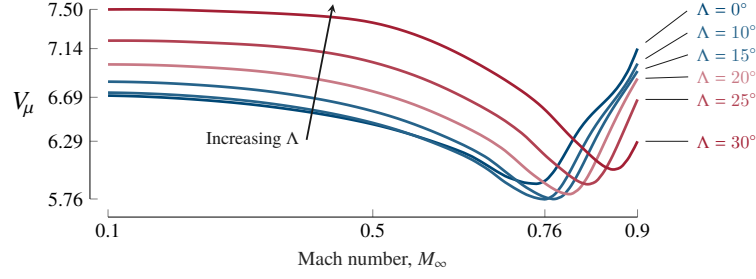
$$\bar{r}_{\text{eng}}^2 = \frac{4 \bar{I}_{\text{eng}}}{m_{\text{eng}} c_{\text{smc}}^2} \quad (16b)$$

$$\eta_{\text{eng}} = \frac{y_{\text{eng}}}{b} \quad (16c)$$

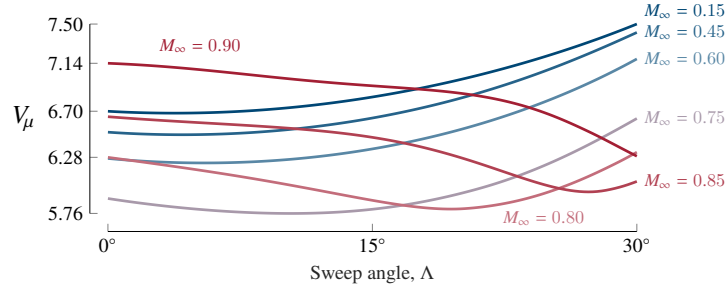
$$\xi_{\text{eng},x} = \frac{\Delta x_{\text{eng}}}{c_{\text{smc}}} \quad (16d)$$

$$\xi_{\text{eng},z} = \frac{\Delta z_{\text{eng}}}{c_{\text{smc}}} \quad (16e)$$

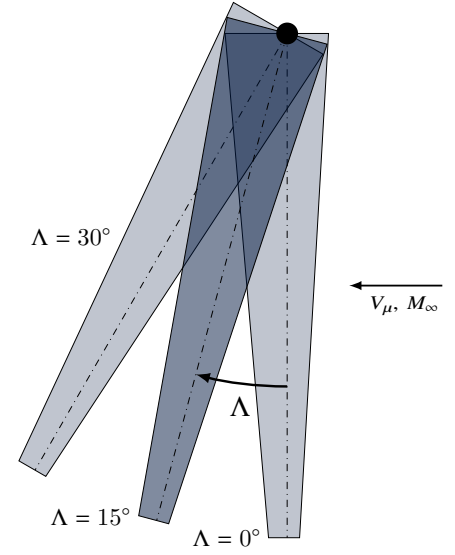




(a) Flutter speed index versus Mach number



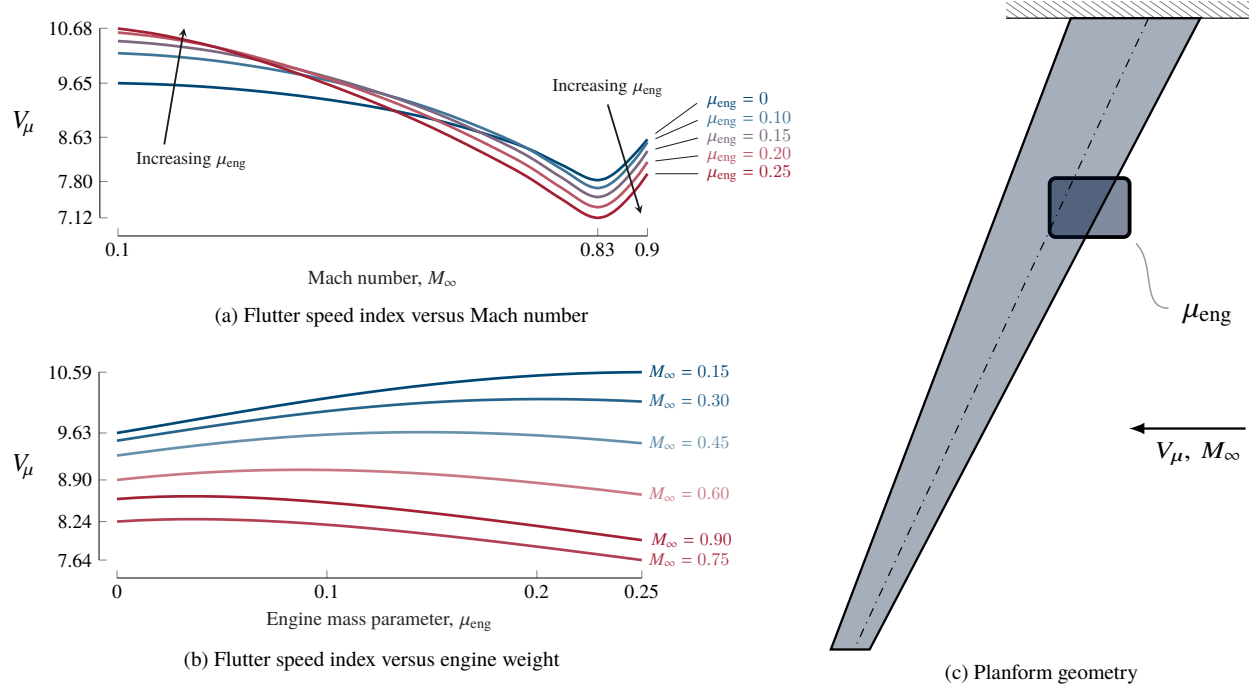
(b) Flutter speed index versus sweep angle



(c) For these results, the wing planform is constant and the sweep angle only changes the orientation with respect to the freestream.

**Fig. 13 Influence of wing sweep angle on the flutter boundary for  $\mathcal{R} = 15$ ,  $\lambda = 0.3$ ,  $\mu = 40$ ,  $\omega_\theta/\omega_h = 35$ ,  $r_\theta^2 = 0.125$ ,  $(x_{ea}/c) = 0.400$ ,  $(x_{cg}/c) = 0.401$ ,  $\tau = 0.14$ , and  $c_{\ell_0} = 0.6$  (C-airfoil family).**

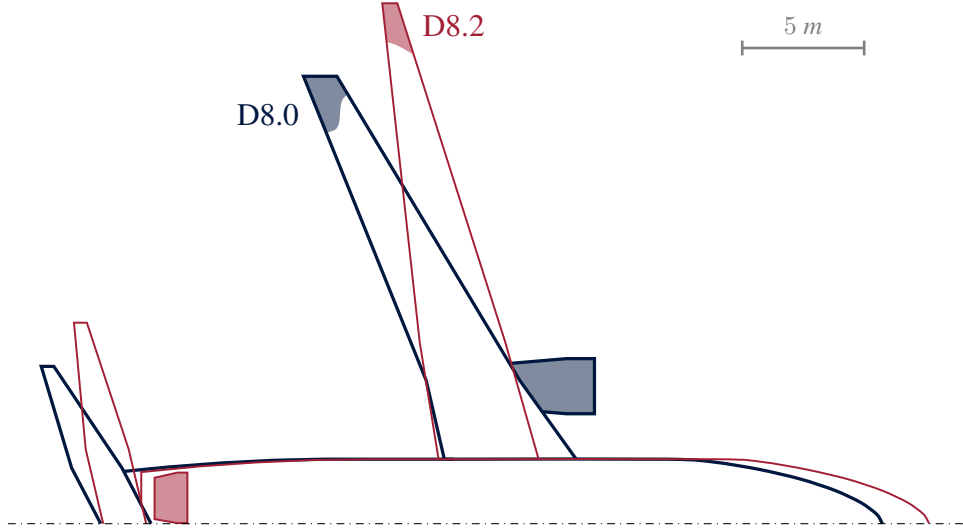
The influence of the mass of the engine on the flutter boundary is shown in Fig. 14. It is expected that adding engine mass for subsonic flow conditions increases the flutter speed, as the mass of the whole system is increased and the inertial loads increase compared to the aerodynamic loads. However, we observe a similar reversal of trends between low subsonic and transonic flows as for wing sweep; for low subsonic flows the additional mass of the engine increases the flutter speed, whereas for transonic conditions the additional mass suddenly decreases the flutter speed. The location of the transonic dip, however, does not change between different engine masses, the only difference is that the dip gets stronger for higher engine masses.



**Fig. 14** Influence of engine weight and freestream Mach number on the flutter boundary for  $\mathcal{R} = 15$ ,  $\lambda = 0.3$ ,  $\Lambda = 25^\circ$ ,  $\mu = 25$ ,  $\omega_\theta/\omega_h = 35$ ,  $r_\theta^2 = 0.125$ ,  $(x_{\text{ea}}/c) = 0.350$ ,  $(x_{\text{cg}}/c) = 0.351$ ,  $\tau = 0.13$ ,  $c_{\ell_0} = 0.6$  (C-airfoil family),  $\eta_{\text{eng}} = 1/4$ ,  $\xi_{\text{eng},x} = -1/4$ ,  $\xi_{\text{eng},z} = -1/8$ ,  $r_{\text{eng},xx}^2 = 0.5$ ,  $r_{\text{eng},yy}^2 = 0.3$ , and  $r_{\text{eng},zz}^2 = 0.3$  (off-diagonal terms zero).

### V.B. Weight-Converged Aircraft

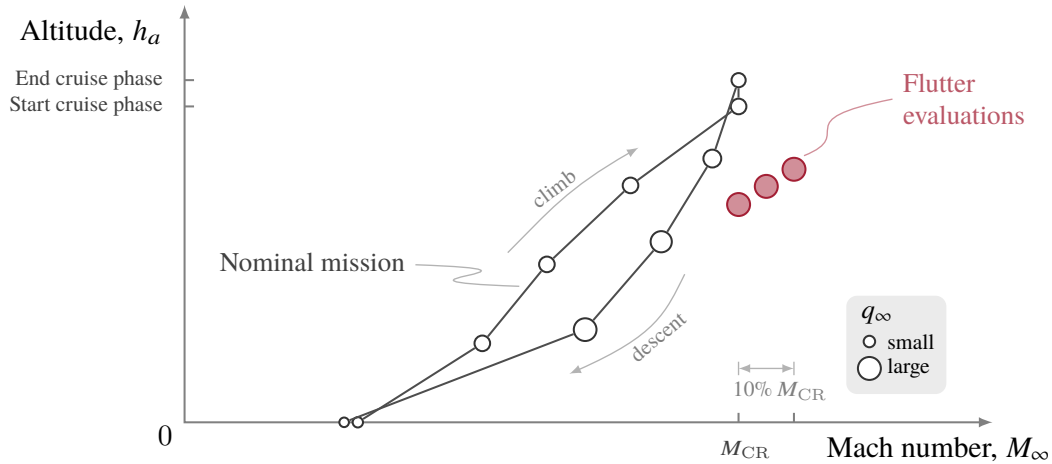
The results in Section V.A showed the influence of wing parameters on the flutter boundary for a wing clamped to a wall. However, for an aircraft design, any change in parameter of the wing cascades through the entire aircraft design, because the aircraft has to be weight converged. In other words, the lift the wing generates has to be equal to the weight of the aircraft. When this is taken into account, the flutter characteristics as a function of wing parameters also change. This section shows the influence of wing parameters on the flutter damping values while ensuring that the aircraft design is weight-converged at each flutter evaluation. These aircraft designs are generated using TASOPT.



**Fig. 15 Comparison of D8.0 and D8.2 configurations [2].**

We consider two different D8.x aircraft configurations, as described in Ref. [2]. The D8.0 and D8.2 configurations are compared in Fig. 15. The D8.0 is a “fuselage-only” modification to the Boeing 737, keeping the wing the same as for the 737—the engines therefore hang under the wing. The D8.2 is different from the D8.0 in two major ways: the engines are moved to the back of the fuselage to enable boundary layer ingestion and the cruise Mach number is reduced to allow for a lower-sweep wing.

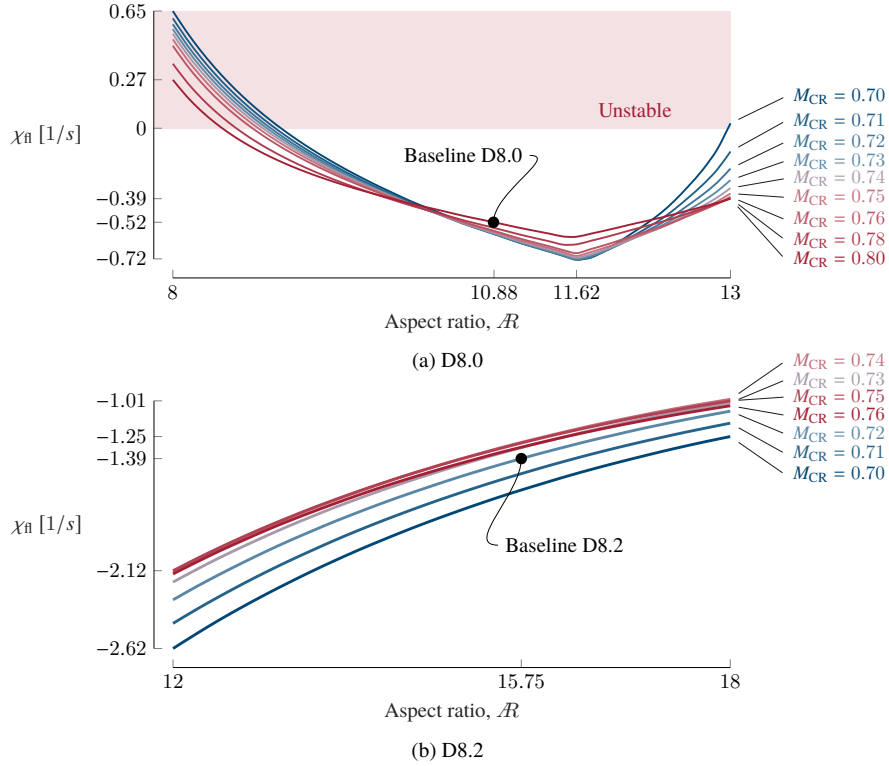
Flutter is evaluated for several worst-case points on the  $(M_\infty, h_a)$  envelope, as shown in Fig. 16. All of the flutter evaluation points are for the never-exceed dynamic pressure, because an increase in dynamic pressure always results in the wing being closer to flutter, even in transonic flight. Due to the transonic dip behavior, it is not clear which freestream Mach number is the worst-case for flutter. Therefore several Mach numbers between the cruise Mach number and 10% above the cruise Mach number are sampled. For each flutter evaluation point we also consider empty wing fuel tanks, half-full wing fuel tanks, and full wing fuel tanks, because these change the mass and center of gravity of the wing substantially.



**Fig. 16  $(M_\infty, h_a)$  envelope for the D8.2 aircraft.**

Fig. 17 shows the aeroelastic eigenvalues as function of wing aspect ratio  $\mathcal{AR}$  and cruise Mach number  $M_\infty$ . Note that  $\chi_{fl} > 0$  indicates flutter. These results consider a freestream Mach number 10% higher than  $M_{CR}$  and full wing tanks as the flutter evaluation point. Note that the trends differ between the different flutter evaluation points shown in Fig. 16, but the one shown in Fig. 17 is one of worst cases. We see that the D8.0 and D8.2 have wildly different values

for  $\chi_{fl}$ , while the trends are also dissimilar. For the D8.2 the increase in aspect ratio leads to an increase in  $\chi_{fl}$  (i.e., closer to instability), whereas for the D8.0 the aspect ratio at first decreases  $\chi_{fl}$  but for higher aspect ratios this trend reverses. The trend for the D8.2 is therefore similar to the results for the clamped wing configuration in Fig. 12, where a higher aspect ratio decreases the flutter speed because the wing is more flexible for higher aspect ratios. For the D8.0, the wing also becomes more flexible for larger aspect ratios, but the engine also moves further outboard. For lower aspect ratios, putting the engine further outward moves the wing towards stability. However, for higher aspect ratios the effect of the larger flexibility in the wing again moves the wing away from stability. An increase in design cruise Mach number puts the D8.2 closer to instability. However, for the D8.0 for lower aspect ratios the cruise Mach number decreases  $\chi_{fl}$ , whereas for aspect ratios around  $\mathcal{AR} = 11$  higher cruise Mach numbers increase  $\chi_{fl}$ .



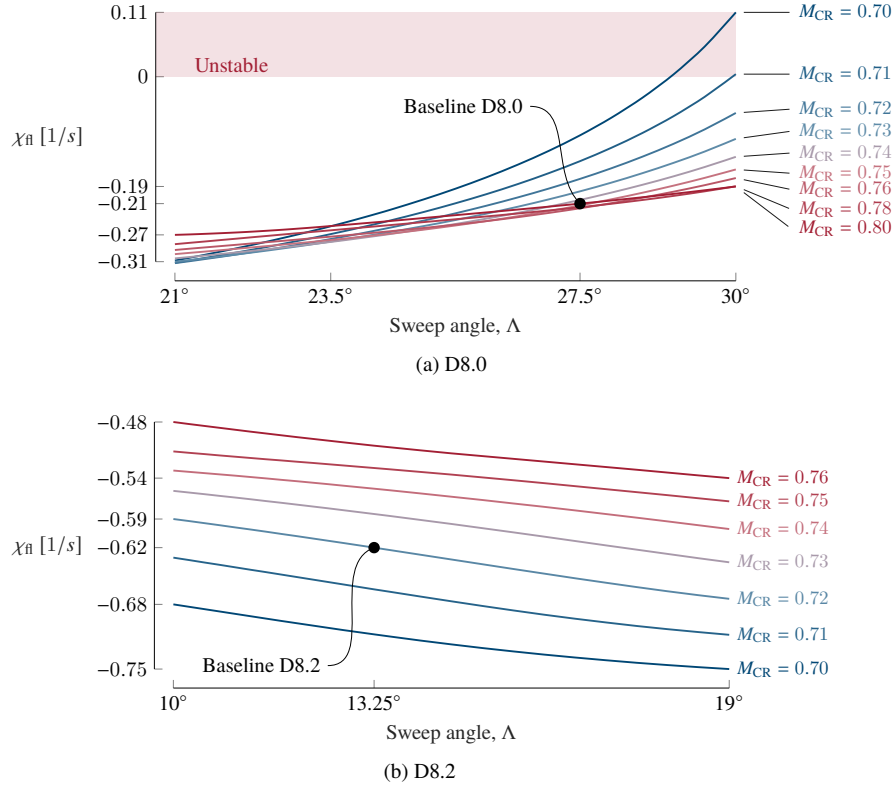
**Fig. 17 Influence of aspect ratio  $\mathcal{AR}$  on maximum aeroelastic eigenvalue  $\chi_{fl}$  for two different aircraft; the D8.0 has a wing with a large sweep angle and wing-mounted engines, the D8.2 has a lower-sweep wing and fuselage-mounted engines. These results are for a flutter evaluation at  $M_\infty = 1.10M_{CR}$  with full wing fuel tanks.**

Fig. 18 shows the aeroelastic eigenvalues of weight-converged aircraft designs for different sweep angles of the wing  $\Lambda$  and different design cruise Mach numbers  $M_{CR}$ . These results consider a freestream Mach number 10% higher than  $M_{CR}$  and empty wing tanks as the flutter evaluation point. The results for the D8.2 show that an increase in sweep angle moves the design away from instability, as does a decrease in cruise Mach number. For the D8.0, however, these trends are mostly reversed, showing the large influence of the inertia and mass of the engine on wing flutter. As explained in Section II.C, with an increase in sweep angle,  $\Delta \bar{x}_{eng}$  decreases and  $\Delta \bar{y}_{eng}$  increases. The additional stability from changing the engine position therefore outweighs the push towards instability by the increase in sweep angle.

## VI. Influence of Transonic Flutter on Aircraft Designs

This section discusses the influence of transonic flutter on next-generation aircraft designs. We will focus here on several variants of the D8.0. All results in this section are generated with TASOPT, using the flutter evaluation points as described in Fig. 16.

First, we show the influence of transonic flutter on the planform design of an advanced-technology version of the D8.0 (Fig. 19). The flutter constraints essentially serve as a span constraint, as we have already seen that higher aspect



**Fig. 18** Influence of sweep angle  $\Lambda$  on maximum aeroelastic eigenvalue  $\chi_{fl}$  for two different aircraft; the D8.0 has a wing with a large sweep angle and wing-mounted engines, the D8.2 has a lower-sweep wing and fuselage-mounted engines. These results are for a flutter evaluation at  $M_\infty = 1.10M_{CR}$  with empty wing fuel tanks.

ratios lead to lower flutter speeds in Fig. 12. Due to the lower aspect ratio, the flutter-constrained design has worse aerodynamic performance, and therefore a 3.3% higher fuel burn. The lower span does result in a lower maximum take-off weight, but that does not offset the higher fuel burn due to poorer aerodynamic performance.

Furthermore, the difference between a D8.0 design using our flutter model and a D8.0 design using a linear flutter model with a Prandtl-Glauert correction [47] is stark (Fig. 19). The design with the linear flutter model has a lower fuel burn compared to the design using our flutter model, while its maximum take-off weight is 3% higher. Arguably more important, however, is the fact that the wing designed with the linear flutter was optimistic and actually missed the (true) transonic flutter constraint, and is therefore not feasible from a flutter standpoint. This example highlights the need for an accurate transonic flutter model.

Second, we investigate specifically the influence of newer material technology on the performance of the D8.0 and describe the influence of transonic flutter constraints on this design. The specific allowable stress is used as a surrogate for new material technology, which is quantified here by a factor multiplying the baseline value, corresponding to aluminum in this case. The varying planform designs and influence on fuel burn and maximum take-off weight are shown in Fig. 20 for specific allowable stress up to 50% higher values than aluminum.

As expected, an increase in specific allowable stress results in a lower fuel burn and maximum take-off weight, which was already observed by Drela [48] for Boeing 737-class aircraft. The inclusion of the flutter constraints limits the efficiency gains seen by an increase in specific allowable stress; without a flutter constraint, a 50% increase in specific allowable stress decreases the fuel burn by as much as 12%, whereas the fuel burn decreases by “only” 10% when a flutter constraint is included. The fuel efficiency gains from better material properties are therefore limited by flutter constraints, since the aspect ratio is limited to mitigate flutter. The lower aspect ratio results in higher induced drag and therefore lower lift-to-drag ratios. As already observed in Fig. 19, the lower aspect ratio does result in a lower maximum take-off weight, but the fuel burn is still higher than for the design without flutter constraints. The trends in

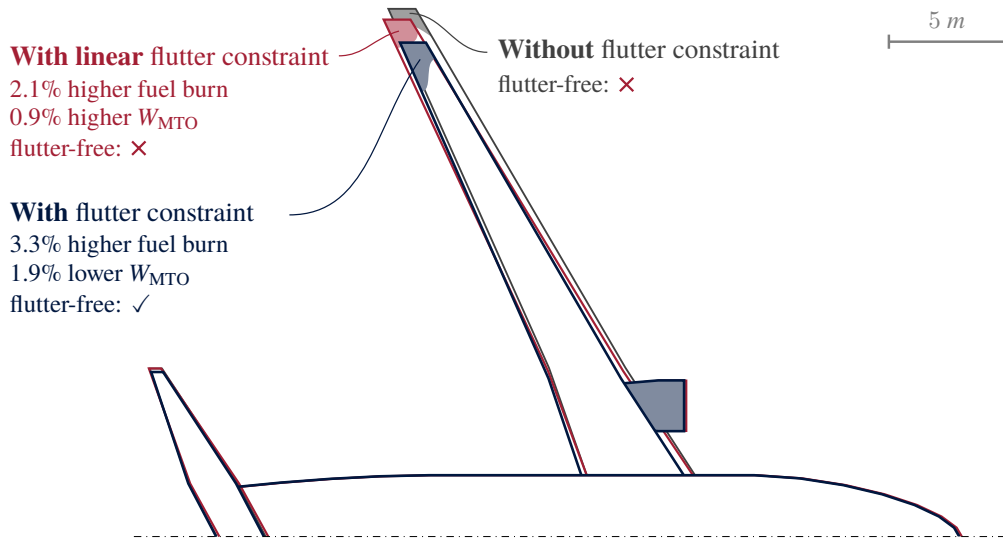


**Fig. 19** Advanced-technology D8.0 designed (1) with our transonic flutter model, (2) with a linear flutter model, and (3) without flutter constraints.

Fig. 20 are similar to those described by Drela [48] for the Boeing 737-class aircraft with and without a span constraint.

## VII. Conclusion

A transonic flutter model applicable to high-aspect ratio swept wings was presented in this paper. This work extends a previously developed 2D transonic flutter model to 3D and implements it in a conceptual design tool. This model discretizes the wing in several sections and builds an aeroelastic system for the whole wing using calibrated flutter coefficients for transonic flow. Such a system is relatively low-dimensional, allowing for fast computation of the eigenvalues, making it applicable for use in a conceptual design tool. The approach is demonstrated to find transonic flutter boundaries for several wing configurations, showing the influences of Mach number, taper ratio, and sweep.

The model is also used to investigate the aeroelastic characteristics of different aircraft designs. The flutter behavior for two different aircraft configurations—one with a high-sweep wing with an engine attached below, one low-sweep wing with no engines attached to the wing—is quite different, and several trends of flutter damping values with respect to wing design parameters are reversed between the two configurations. For example, a larger sweep angle pushes the aircraft with wing-mounted engines towards instability, whereas for the aircraft with fuselage-mounted engines a larger sweep angle moves the design away from instability. Furthermore, it was found that the inclusion of flutter constraints in the aircraft design optimization limits the aspect ratio of the wings, resulting in higher fuel burn. For the case studied, a linear flutter model failed to impose the appropriate constraints and the resulting design was not flutter-free. Transonic flutter is shown to limit the performance gains seen by using more advanced materials in the wing. Note that these trends are not generally applicable to any aircraft design; the onset of flutter is quite subtle and is sensitive to small changes in wing geometry, engine parameters, or aerodynamic forces. It is therefore crucial to include an accurate, fast aeroelastic analysis early in the conceptual design phase.

## Funding Sources

This work was supported in part by the NASA LEARN program grant number NNX14AC73A and the SUTD-MIT International Design Center.

## References

- [1] Bradley, M. K., and Droney, C. K., “Subsonic Ultra Green Aircraft Research: Phase I Final Report,” Tech. Rep. NASA/CR–2011-216847, National Aeronautics and Space Administration (NASA), Boeing Research & Technology, Huntington Beach, California,

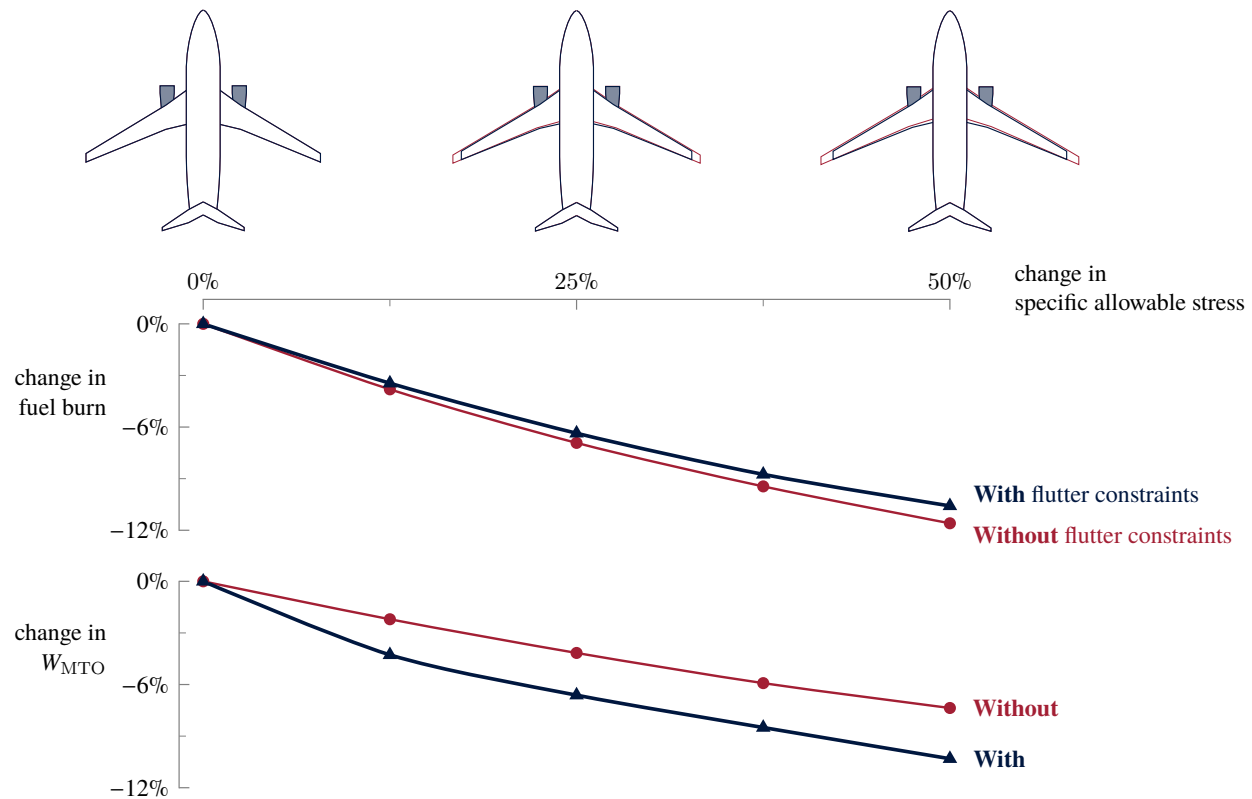


**Fig. 20** Variations of optimum fuel burn and maximum take-off weight with specific allowable stress.

April 2011.

- [2] Drela, M., "Development of the D8 Transport Configuration," *29th AIAA Applied Aerodynamics Conference*, Honolulu, Hawaii, 2011. doi:10.2514/6.2011-3970.
- [3] Bendiksen, O. O., "Review of unsteady transonic aerodynamics: theory and applications," *Progress in Aerospace Sciences*, Vol. 47, No. 2, 2011, pp. 135–167.
- [4] Doggett Jr, R. V., Morgan, H. G., and Rainey, A., "An Experimental Investigation of Aerodynamic Effects of Airfoil Thickness on Transonic Flutter Characteristics," Tech. Rep. TM X-79, National Aeronautics and Space Administration (NASA), Langley Research Center, Langley Field, Virginia, nov 1959.
- [5] Farmer, M., and Hanson, P., "Comparison of Supercritical and Conventional Wing Flutter Characteristics," *17th Structures, Structural Dynamics, and Materials Conference*, American Institute of Aeronautics and Astronautics, 1976. doi:10.2514/6.1976-1560.
- [6] Mykytow, W. J., "A Brief Overview of Transonic Flutter Problems," *44th Meeting of the AGARD Structures and Materials Panel*, Lisbon, Portugal, 1977, pp. 11–1 – 11–11.
- [7] Edwards, J. W., Bennett, R. M., Whitlow, W., and Seidel, D. A., "Time-Marching Transonic Flutter Solutions Including Angle-of-Attack Effects," *Journal of Aircraft*, Vol. 20, No. 11, 1983, pp. 899–906. doi:10.2514/3.48190.
- [8] Reddy, T., Srivastava, R., and Kaza, K., "The Effects of Rotational Flow, Viscosity, Thickness, and Shape on Transonic Flutter Dip Phenomena," *29th Structures, Structural Dynamics and Materials Conference*, American Institute of Aeronautics and Astronautics, 1988. doi:10.2514/6.1988-2348.
- [9] Bendiksen, O. O., and Kousen, K. A., "Transonic Flutter Analysis using the Euler Equations," *28th Structures, Structural Dynamics and Materials Conference*, American Institute of Aeronautics and Astronautics, 1987. doi:10.2514/6.1987-911.
- [10] Theodorsen, T., "General Theory of Aerodynamic Instability and the Mechanism of Flutter," Tech. Rep. NACA-TR-496, National Aeronautics and Space Administration (NASA), Langley Aeronautical Lab, Hampton, Virginia, January 1935.

- [11] Barmby, J. G., Cunningham, H. J., and Garrick, I. E., "Study of Effects of Sweep on the Flutter of Cantilever Wings," Tech. Rep. 104, National Advisory Committee for Aeronautics (NACA), Langley Aeronautical Laboratory, Langley Field, Virginia, 1951.
- [12] Yates, E. C., "Modified-Strip-Analysis Method for Predicting Wing Flutter at Subsonic to Hypersonic speeds," *Journal of Aircraft*, Vol. 3, No. 1, 1966, pp. 25–29. doi:10.2514/3.43702.
- [13] Liu, F., Cai, J., Zhu, Y., Wong, A., and Tsai, H., "Calculation of Wing Flutter by a Coupled CFD-CSD Method," *38th Aerospace Sciences Meeting and Exhibit*, American Institute of Aeronautics and Astronautics, 2000. doi:10.2514/6.2000-907.
- [14] Bhatia, M., and Beran, P., "Higher-Order Transonic Flutter Predictions," *AIAA Journal*, Vol. 55, No. 11, 2017, pp. 3881–3890. doi:10.2514/1.j055930.
- [15] ZWAAN, R. J., "Verification of calculation methods for unsteady airloads in the prediction of transonic flutter," *Journal of Aircraft*, Vol. 22, No. 10, 1985, pp. 833–839. doi:10.2514/3.45212.
- [16] Chen, P. C., Sarhaddi, D., and Liu, D. D., "Transonic-Aerodynamic-Influence-Coefficient Approach for Aeroelastic and MDO Applications," *Journal of Aircraft*, Vol. 37, No. 1, 2000, pp. 85–94. doi:10.2514/2.2565.
- [17] Kennedy, G., Kenway, G., and Martins, J., "Towards Gradient-Based Design Optimization of Flexible Transport Aircraft with Flutter Constraints," *15th AIAA/ISSMO Multidisciplinary Analysis and Optimization Conference*, Atlanta, Georgia, 2014. doi:10.2514/6.2014-2726.
- [18] Mallik, W., Kapania, R. K., and Schetz, J. A., "Effect of Flutter on the Multidisciplinary Design Optimization of Truss-Braced-Wing Aircraft," *Journal of Aircraft*, Vol. 52, 2015. doi:10.2514/1.c033096.
- [19] Opgenoord, M. M. J., Drela, M., and Willcox, K. E., "Physics-Based Low-Order Model for Transonic Flutter Prediction," *AIAA Journal*, Vol. 56, No. 4, 2018, pp. 1519–1531. doi:10.2514/1.J056710.
- [20] Proctor, J. L., Brunton, S. L., and Kutz, J. N., "Dynamic Mode Decomposition with Control," *SIAM Journal on Applied Dynamical Systems*, Vol. 15, No. 1, 2016, pp. 142–161. doi:10.1137/15m1013857.
- [21] Bisplinghoff, R. L., Ashley, H., and Halfman, R. L., *Aeroelasticity*, Dover Publications, New York, 1996.
- [22] Dowell, E. H., *A Modern Course in Aeroelasticity*, Springer, Cham, 2014.
- [23] Kier, T. M., "Comparison of Unsteady Aerodynamic Modelling Methodologies with Respect to Flight Loads Analysis," *AIAA Atmospheric Flight Mechanics Conference and Exhibit*, San Francisco, California, 2005. doi:10.2514/6.2005-6027.
- [24] Fung, Y. C., *An Introduction to the Theory of Aeroelasticity*, Dover Publications, Inc., 1993.
- [25] Wright, J. R., and Cooper, J. E., *Introduction to Aircraft Aeroelasticity and Loads*, Wiley, Chichester, West Sussex, England, 2015.
- [26] Albano, E., and Rodden, W. P., "A Doublet-Lattice Method for Calculating Lift Distributions on Oscillating Surfaces in Subsonic Flows," *AIAA journal*, Vol. 7, No. 2, 1969, pp. 279–285. doi:10.2514/3.5086.
- [27] Katz, J., and Plotkin, A., *Low-Speed Aerodynamics*, Cambridge University Press, 2001.
- [28] Murua, J., Palacios, R., and Graham, J. M. R., "Applications of the Unsteady Vortex-Lattice Method in Aircraft Aeroelasticity and Flight Dynamics," *Progress in Aerospace Sciences*, Vol. 55, 2012, pp. 46–72. doi:10.1016/j.paerosci.2012.06.001.
- [29] Drela, M., "ASWING 5.99 Technical Description – Unsteady Extension," Tech. rep., Massachusetts Institute of Technology (MIT), Cambridge, Massachusetts, March 2015.
- [30] Patil, M., and Hodges, D., "On the Importance of Aerodynamic and Structural Geometrical Nonlinearities in Aeroelastic Behavior of High-Aspect-Ratio Wings," *41st Structures, Structural Dynamics, and Materials Conference and Exhibit*, American Institute of Aeronautics and Astronautics, 2000. doi:10.2514/6.2000-1448.
- [31] Tang, D., and Dowell, E. H., "Experimental and Theoretical Study on Aeroelastic Response of High-Aspect-Ratio Wings," *AIAA Journal*, Vol. 39, 2001, pp. 1430–1441. doi:10.2514/3.14886.
- [32] Economou, T. D., Palacios, F., Copeland, S. R., Lukaczyk, T. W., and Alonso, J. J., "SU2: An Open-Source Suite for Multiphysics Simulation and Design," *AIAA Journal*, Vol. 54, No. 3, 2016, pp. 828–846. doi:10.2514/1.J053813.



- [33] Bennett, R. M., “Test Cases for Flutter of the Benchmark Models Rectangular Wings on the Pitch and Plunge Apparatus,” Tech. rep., Aeroelasticity Branch, Structures and Materials, National Aeronautics and Space Administration (NASA), Langley Research Center, Hampton, Virginia, 2000.
- [34] Heeg, J., “Overview and Lessons Learned from the Aeroelastic Prediction Workshop,” *54th AIAA/ASME/ASCE/AHS/ASC Structures, Structural Dynamics, and Materials Conference*, Boston, Massachusetts, 2013. doi:10.2514/6.2013-1798.
- [35] Heeg, J., Chwalowski, P., Raveh, D. E., Jirasek, A., and Dalenbring, M., “Overview and Data Comparisons from the 2nd Aeroelastic Prediction Workshop,” *34th AIAA Applied Aerodynamics Conference*, Washington, D.C, 2016. doi:10.2514/6.2016-3121.
- [36] Dansberry, B. E., Durham, M. H., Bennett, R. M., Turnock, D. L., Silva, W. A., and Rivera Jr, J. A., “Physical Properties of the Benchmark Models Program Supercritical Wing,” Tech. Rep. NASA TN 1077, National Aeronautics and Space Administration (NASA), Langley Research Center, Hampton, Virginia, 1993.
- [37] Farmer, M. G., “A Two-Degree-of-Freedom Flutter Mount System with Low Damping for Testing Rigid Wings at Different Angles of Attack,” Tech. Rep. NASA TM 83302, National Aeronautics and Space Administration (NASA), Langley Research Center, Hampton, Virginia, April 1982.
- [38] Chwalowski, P., and Heeg, J., “FUN3D Analyses in Support of the Second Aeroelastic Prediction Workshop,” *34th AIAA Applied Aerodynamics Conference*, Washington, D.C, 2016. doi:10.2514/6.2016-3122.
- [39] Jirásek, A., Dalenbring, M., and Navrátil, J., “Computational Fluid Dynamics Study of Benchmark Supercritical Wing at Flutter Condition,” *AIAA Journal*, Vol. 55, No. 1, 2016, pp. 153–160. doi:10.2514/1.J054916.
- [40] Chwalowski, P., Heeg, J., and Biedron, R. T., “Numerical Investigations of the Benchmark Supercritical Wing in Transonic Flow,” *58th AIAA/ASCE/AHS/ASC Structures, Structural Dynamics, and Materials Conference*, American Institute of Aeronautics and Astronautics, 2017. doi:10.2514/6.2017-0190.
- [41] Drela, M., “N3 Aircraft Concept Designs and Trade Studies – Appendix,” Tech. Rep. NASA CR-2010-216794/VOL2, 2010.
- [42] Greitzer, E. M., “N+3 Aircraft Concept Designs and Trade Studies, Final Report. Volume 1,” Tech. Rep. NASA CR-2010-216794/VOL1, National Aeronautics and Space Administration (NASA), 2010.
- [43] Greitzer, E. M., “N+3 Aircraft Concept Designs and Trade Studies, Final Report. Volume 2: Appendices — Design Methodologies for Aerodynamics, Structures, Weight, and Thermodynamic Cycles,” Tech. Rep. NASA CR-2010-216794/VOL2, National Aeronautics and Space Administration (NASA), 2010.
- [44] Nelder, J. A., and Mead, R., “A Simplex Method for Function Minimization,” *The Computer Journal*, Vol. 7, No. 4, 1965, pp. 308–313. doi:10.1093/comjnl/7.4.308.
- [45] Neill, D. J., Johnson, E. H., and Canfield, R., “ASTROS - A Multidisciplinary Automated Structural Design Tool,” *Journal of Aircraft*, Vol. 27, No. 12, 1990, pp. 1021–1027. doi:10.2514/3.45976.
- [46] Ringertz, U. T., “On Structural Optimization with Aeroelasticity Constraints,” *Structural Optimization*, Vol. 8, No. 1, 1994, pp. 16–23. doi:10.1007/bf01742928.
- [47] Mallik, W., Kapania, R. K., and Schetz, J. A., “Multidisciplinary Design Optimization of Medium-Range Transonic Truss-Braced Wing Aircraft with Flutter Constraint,” *54th AIAA/ASME/ASCE/AHS/ASC Structures, Structural Dynamics, and Materials Conference*, American Institute of Aeronautics and Astronautics, 2013. doi:10.2514/6.2013-1454.
- [48] Drela, M., “Design Drivers of Energy-Efficient Transport Aircraft,” *SAE International Journal of Aerospace*, Vol. 4, No. 2, 2011, pp. 602–618. doi:10.4271/2011-01-2495.